

Tungsten and hafnium distribution in calcium–aluminum inclusions (CAIs) from Allende and Efremovka

Munir Humayun^{a,b,*}, Steven B. Simon^c, Lawrence Grossman^{c,d}

^a National High Magnetic Field Laboratory, Florida State University, 1800 E. Paul Dirac Drive, Tallahassee, FL 32310, USA

^b Department of Geological Sciences, Florida State University, 108 Carraway Building, Tallahassee, FL 32306, USA

^c Department of the Geophysical Sciences, University of Chicago, 5734 S. Ellis Avenue, Chicago, IL 60637, USA

^d Enrico Fermi Institute, University of Chicago, 5640 S. Ellis Avenue, Chicago, IL 60637, USA

Received 14 August 2006; accepted in revised form 13 July 2007; available online 6 August 2007

Abstract

Recent ^{182}Hf – ^{182}W age determinations on Allende Ca-, Al-rich refractory inclusions (CAIs) and on iron meteorites indicate that CAIs have initial $\varepsilon^{182}\text{W}$ (-3.47 ± 0.20 , 2σ) identical to that of magmatic iron meteorites after correction of cosmogenic ^{182}W burn-out (-3.47 ± 0.35 , 2σ). Either the Allende CAIs were isotopically disturbed or the differentiation of magmatic irons (groups IIAB, IID, IIIAB, and IVB) all occurred <1 m.y. after CAI formation. To assess the extent of isotopic disturbance, we have analyzed the elemental distribution of Hf and W in two CAIs, Ef2 from Efremovka (CV3 reduced), and Golfball from Allende (CV3 oxidized). Fassaite is the sole host of Hf (10–25 ppm) and, therefore, of radiogenic W in CAIs, with $^{180}\text{Hf}/^{184}\text{W} > 10^3$, which is lowered by the ubiquitous presence of metal inclusions to $^{180}\text{Hf}/^{184}\text{W} > 10$ in bulk fassaite. Metal alloy (Ni $\sim 50\%$) is the sole host of W (~ 500 ppm) in Ef2, while opaque assemblages (OAs) and secondary veins are the hosts of W in Golfball. A large metal alloy grain from Ef2, EM2, has $^{180}\text{Hf}/^{184}\text{W} < 0.006$. Melilite has both Hf and W below detection limits (<0.01 ppm), but the presence of numerous metallic inclusions or OAs makes melilite a carrier for W, with $^{180}\text{Hf}/^{184}\text{W} < 1$ in bulk melilite. Secondary processes had little impact on the ^{182}Hf – ^{182}W systematics of Ef2, but a vein cross-cutting fassaite in Golfball has >100 ppm W with no detectable Pt or S. This vein provides evidence for transport of oxidized W in the CAI. Because of the ubiquitous distribution of OAs, interpretations of the ^{182}Hf – ^{182}W isochron reported for Allende CAIs include: (i) all W in the OAs was derived by alteration of CAI metal, or (ii) at least some of the W in OAs may have been equilibrated with radiogenic W during metamorphism of Allende. Since (ii) cannot be ruled out, new ^{182}Hf – ^{182}W determinations on CAIs from reduced CV3 chondrites are needed to firmly establish the initial W isotopic composition of the solar system.

© 2007 Elsevier Ltd. All rights reserved.

1. INTRODUCTION

The ^{182}Hf – ^{182}W system ($t_{1/2} = 9$ Ma) is an important new extinct radionuclide chronometer for dating metal–silicate fractionation in the early solar system and during planetary core formation (Harper et al., 1996; Lee and Halliday, 1996; Kleine et al., 2002; Yin et al., 2002). Two

key pieces of information are essential for interpretation of the chronometer: (1) the initial $\varepsilon^{182}\text{W}$, where $\varepsilon^{182}\text{W}$ is defined as,

$$\varepsilon^{182}\text{W} = \left[\frac{(^{182}\text{W}/^{184}\text{W})_{\text{sample}}}{(^{182}\text{W}/^{184}\text{W})_{\text{std}}} - 1 \right] \times 10^4$$

where $(^{182}\text{W}/^{184}\text{W})_{\text{std}}$ is the isotopic composition of W in a terrestrial standard (e.g., Kleine et al., 2005a), and (2) the initial $^{182}\text{Hf}/^{180}\text{Hf}$, both of which can be obtained from an isochron. Since the inception of ^{182}Hf – ^{182}W dating, the

* Corresponding author. Fax: +1 850 644 0827.

E-mail address: humayun@magnet.fsu.edu (M. Humayun).

solar system initial $\epsilon^{182}\text{W}$ has been derived from iron meteorites (Harper et al., 1996; Lee and Halliday, 1996). It is evident that iron meteorites must have formed after the first condensed materials were accumulated into protoplanetary bodies, that the bodies subsequently differentiated, and that their $\epsilon^{182}\text{W}$ record metal–silicate differentiation after the formation of the earliest condensed materials. As such, iron meteorites formed within a significant fraction of the half-life of ^{182}Hf , so that the use of their initial $^{182}\text{W}/^{184}\text{W}$ as the solar system value is driven more by expedience than by appropriateness.

It has been generally accepted that Ca-, Al-rich refractory inclusions (CAIs) represent the earliest condensed materials from the solar system (Grossman, 1972; Gray et al., 1973). This has been confirmed by precise U–Pb chronology (Amelin et al., 2002a,b). Thus, it is surprising that the determination of the ^{182}Hf – ^{182}W isochron for Allende CAIs by Kleine et al. (2005a) resulted in an initial $\epsilon^{182}\text{W}$ (-3.47 ± 0.20) that is more radiogenic than the weighted average initial $\epsilon^{182}\text{W}$ of magmatic iron meteorites (-3.79 ± 0.06) measured in the same lab. Corrections for cosmogenic effects on W isotopes reduced this mean value to -3.47 ± 0.35 , 2σ , for five iron meteorites representing groups IIAB, IID, IIIAB, and IVB (Markowski et al., 2006a). This leads to a time interval of formation of iron meteorites in four magmatic iron groups of <1 m.y. after formation of CAIs, a time that precedes the assembly of chondrites (Kleine et al., 2005a; Markowski et al., 2006a,b). Since there is no other way to independently determine the age of magmatic iron meteorites precisely enough to test the ^{182}Hf – ^{182}W chronology, the acceptance of the Kleine et al. (2005a) findings must be based on an examination of the robustness of the ^{182}Hf – ^{182}W isochron reported for Allende CAIs.

There are three possible explanations of the measured $\epsilon^{182}\text{W}$ discrepancy between CAIs and magmatic iron meteorites: (1) small nuclear anomalies in W from magmatic iron meteorites (or from CAIs) that contribute to the apparent deficiency (excess, in the case of CAIs) of ^{182}W , analogous to the endemic nuclear anomalies reported in Mo and Ru (Chen et al., 2004; Papanastassiou et al., 2004; cf. Brandon et al., 2005); (2) cosmic-ray neutron capture burnout of ^{182}W in iron meteorites; and (3) disturbance of the ^{182}Hf – ^{182}W isochron in Allende CAIs that may have imparted a radiogenic $\epsilon^{182}\text{W}$ in Allende CAIs during parent body processes that occurred after chondrule formation and subsequent parent body assembly. Were nuclear effects (1) to account for the discrepancy, the application of the ^{182}Hf – ^{182}W chronometer to iron meteorites would be compromised. New measurements by Markowski et al. (2006a,b) help constrain the cosmic-ray neutron burnout (2), but support a very early differentiation of magmatic iron meteorites. This leads us to examine the impact of alteration effects in Allende CAIs (3) on their ^{182}Hf – ^{182}W systematics. Palme et al. (1994) showed that W was depleted in the refractory metal of opaque assemblages (OAs) in Allende inclusion Egg-6, and concentrated in surrounding silicates. Campbell et al. (2003) measured the distribution of siderophile elements, including W, in CAI metal from the CV3 carbonaceous chondrites Allende and

Efremovka. They reported high concentrations of Ru, Rh, W, Re, and Os in a sulfide vein cross-cutting a refractory inclusion, Allende TS68. They also documented the depletion of W in CAI metal in Efremovka. Such effects occurred during parent body metamorphism and alteration of the carbonaceous chondrites. However, as appreciated by Kleine et al. (2005a), the release of unradiogenic tungsten from CAI metal and its infiltration into adjacent silicate phases is insufficient proof that radiogenic tungsten from silicates isotopically exchanged with W in refractory metal nuggets resulting in rotation of the ^{182}Hf – ^{182}W isochron.

To provide a better understanding of both the primary and secondary distribution of Hf and W in CAIs from CV3 carbonaceous chondrites, we undertook a laser ablation ICP-MS study of CAIs from Allende and Efremovka. Allende belongs to the oxidized subgroup of the CV3 carbonaceous chondrites, while Efremovka belongs to the reduced subgroup (Sylvester et al., 1993). Allende CAIs have experienced more significant alteration and low-grade metamorphism, than those in Efremovka. Much Fe–Ni metal in Allende CAIs has been altered to magnetite, sulfide, and refractory metal nuggets (El Goresy et al., 1978; Blum et al., 1989; Palme et al., 1994), while that of Efremovka remains Fe–Ni alloy, with minor amounts of V-magnetite and sulfide (Fisenko et al., 1992; Campbell et al., 2003). Sylvester et al. (1993) reported correlated enrichments in the volatile elements Na and Au in bulk CAIs from Allende, relative to CAIs from Efremovka and other reduced CV3 subgroup chondrites. Our previous study (Campbell et al., 2003) focused on the metal in CAIs and, aside from the single sulfide vein reported in TS68, provided no data on the distribution of siderophile elements in the non-metal portions of the CAIs. Further, there is little information on the distribution of Hf and W between the primary phases of CAIs: melilite, fassaite, spinel, and metal. In this study, we emphasize elemental distribution in melilite, fassaite, and spinel, and examine W redistribution in the vicinity of metal–silicate contacts. Humayun et al. (2006) reported preliminary results of this study.

2. SAMPLES AND ANALYTICAL METHODOLOGY

Section GBS of the Allende inclusion Golfball, an unusual Type B inclusion described by Simon et al. (2005), and Efremovka CAI Ef2 (Fisenko et al., 1992) were studied. Allende GBS contains a prominent spinel palisade body, a region of the inclusion enclosed in a shell of spinel, seen in thin section as a complete ring, which has a higher level of refractory metal grains than the remainder of GBS and was targeted in this study. Ef2, a Compact Type A (melilite-rich, coarse-grained refractory inclusion), contains a large ~ 300 μm diameter refractory metal spherule, EM2 (Fisenko et al., 1992). Campbell et al. (2003) described the siderophile element composition of metal in Ef2, including EM2, in detail. In both inclusions, melilite, fassaite and spinel are the dominant minerals with abundant refractory metal grains (Efremovka) or opaque assemblages (Allende).

All measurements reported here were performed on a New Wave UP213 laser ablation system coupled to a Finnigan Element™ ICP-MS at the NHMFL Plasma Analytical

Facility. The UP213 is a frequency-quintupled Nd-YAG laser (213 nm UV) with a power output of 4 mJ, an aperture-controlled spot-size (4–100 μm), and computer-controlled movable X–Y–Z stage with submicron spatial resolution. The 213 nm laser couples better to silicates than the 266 nm laser used in our previous work (Campbell and Humayun, 1999; Campbell et al., 2003). Aerosol is transported from the ablation cell by a flow of He (800 ml/min) with additional Ar (~ 1000 ml/min) make-up gas. Unlike our previous set-up with a CETAC LSX-200 (Campbell and Humayun, 1999), the UP213 is not fitted with a spray chamber and the amount of dead volume in the UP213 ablation cell is smaller than that of the LSX-200 ablation cell. Consequently, the rise time of the signal is much sharper, the wash-out shorter (2–4 vs. 10–20 s) and the spatial resolution is improved. Measurements were performed in line scan mode with 12 or 25 μm beam diameters, with the stage moved at 4–5 $\mu\text{m/s}$, 10 Hz laser repetition rate and 50% power output (~ 0.03 mJ). The peaks ^7Li , ^{25}Mg , ^{27}Al , ^{29}Si , ^{34}S , ^{43}Ca , ^{49}Ti , ^{53}Cr , ^{57}Fe , ^{60}Ni , ^{180}Hf , ^{181}Ta , ^{182}W , ^{183}W , ^{193}Ir , ^{195}Pt , and ^{197}Au were acquired in low resolution ($R = 300$) at 50 ms/peak. All major element peaks (except Na) for CAI minerals were determined to identify the phases being ablated and to determine their compositions. Intensities of two W peaks were determined to ensure that our measurements were not compromised by unantic-

ipated interferences. An isobaric interference from ^{180}W (0.12%) on ^{180}Hf (35.1%) was corrected by monitoring ^{182}W (26.49%). Standards used to convert intensities to concentrations included the NIST SRM 612, a silicate glass doped with a suite of trace elements at ~ 40 ppm (Pearce et al., 1997; Sylvester and Eggins, 1997), NIST SRM 1263a steel, the MPI-DING glasses, KL2-G, ML3B-G, GOR128-G (Jochum et al., 2000, 2006), and the iron meteorites North Chile (Filomena specimen) IIA and Hoba IVB (Wasson et al., 1989; Campbell et al., 2002). Table 1 gives elemental concentrations and relative sensitivity factors for five standards used in calibrating silicate analyses, and Table 2 provides the same for four standards used for calibrating metal analyses. Relative sensitivity factors (RSF):

$$\text{RSF} = \frac{C_i/C_{\text{SiO}_2}}{I_i/I_{^{29}\text{Si}}} \text{ or } \frac{C_i/C_{\text{Fe}}}{I_i/I_{^{57}\text{Fe}}}$$

(where C_i is the concentration of element i , and I_i is the intensity for the peak used for that element) for each of the elements analyzed were calculated from the concentrations given in Tables 1 and 2 and from measured background-subtracted intensity ratios, and are shown for a representative analytical session. The four MPI-DING glasses provided RSFs normalized to SiO_2 that were mutually consistent, but for most elements are $\sim 22\%$ lower than those obtained from the NIST SRM 612 glass (Table 1).

Table 1
Concentrations and relative sensitivity factors (RSFs) normalized to SiO_2 for use with silicates

	MPI-DING GOR128-G	MPI-DING KL2-G	MPI-DING ML3B-G	MPI-DING T1-G	NIST SRM 612	RSF	SD (%)
<i>Concentrations</i>							
SiO_2 (%)	46.1	50.10	50.90	58.5	71.79		
TiO_2	0.28	2.60	2.09	0.73	0.00803		
Al_2O_3	9.87	13.10	13.40	17	2.11		
FeO	9.78	10.70	10.90	6.42	0.00725		
MgO	25.8	7.26	6.56	3.74	0.0128		
CaO	6.17	10.80	10.50	7.08	11.93		
Cr (ppm)	2180	310	170	22	39.88		
Ni	1070	116	105	13	38.44		
Hf	0.351	4.14	3.32	3.9	34.77		
Ta	—	0.97	0.55	0.45	39.77		
W					40.1		
Pt					2.59		
Au					5		
<i>Relative sensitivity factors</i>							
SiO_2	1.000	1.000	1.000	1.000	1.000	1.000	
TiO_2	0.161	0.159	0.161	0.149	0.236	0.160	1
Al_2O_3	0.0234	0.0231	0.0233	0.0221	0.0354	0.0233	1
FeO	0.330	0.332	0.334	0.315	0.355	0.332	1
MgO	0.157	0.157	0.161	0.149	0.220	0.158	1
CaO	3.42	3.34	3.53	3.17	4.65	3.43	3
Cr	497	542	527	532	548	522	4
Ni	372	365	338	313	368	358	5
Hf	33	37	36	35	49	36	6
Ta	—	17	17	15	23	17	1
$\text{W}(182)$					78	60	
$\text{W}(183)$					144	111	
Pt					107	83	
Au					68	53	

Major element oxides in wt. %, trace elements in ppm. Bold values used to compile average RSF. See text for discussion.

Table 2
Concentrations (ppm) and RSFs normalized to Fe for use with metals

	SRM 612	SRM 1263a	Filomena IIA	Hoba IVB	RSF
Al	11100	2400			
Si	336000	7400			
P	55.16	290			
S	16	57			
Sc	41				
Ti	48	500			
V	39	3100			
Cr	40	13100	68	178	
Fe	56.3	944000	938960	829000	
Co	35.3	480	4540	7800	
Ni	38.4	3200	56500	163900	
Y	38.3				
Mo	38	300		26	
Hf	35	5			
Ta	40	530			
W	40	460	2.562	3.25	
Ir			3.37	29.14	
Pt	2.59		20.7	28.6	
Au	4.58	5	0.612	0.078	
<i>Relative sensitivity factors w.r.t. Fe</i>					
Al	0.074	0.029	—	—	0.074
Si	1.63	1.15	—	—	1.15
P	0.096	0.057	—	—	0.057
S	0.113	0.313	—	—	0.313
Sc	0.040	—	—	—	0.040
Ti	0.610	0.315	—	—	0.315
V	0.0193	0.020	—	—	0.020
Cr	0.192	0.175	0.108	0.188	0.175
Fe	1.52	1.0000	1.0000	1.0000	1.0000
Co	0.0258	0.0264	0.0252	0.0259	0.0258
Ni	0.107	0.112	0.118	0.114	0.114
Y	0.0317	—	—	—	0.032
Mo	0.0920	0.0941	—	0.1044	0.0941
Hf	0.129	0.394	—	—	0.129
Ta	0.0246	0.0265	—	—	0.0265
W	0.0436	0.0445	0.0470	0.0521	0.0470
Ir	—	—	0.0166	0.0187	0.0187
Pt	0.0409	—	0.0425	0.0498	0.0498
Au	0.0143	0.0176	0.0192	0.0205	0.0192

Bold values used to compile average RSF. See text for discussion.

Accordingly, the RSFs used for calibration were obtained from an average of the RSFs of GOR128-G, KL2-G, and ML3B-G (with the exception of Ta in GOR128-G) for all elements except W, Pt, and Au, the abundances of which are not homogeneous in the MPI-DING glasses since the glasses were formed by melting of rock powders in Pt vessels (Jochum et al., 2006). The RSFs for W, Pt, and Au were obtained from NIST SRM 612 (with Pt and Au abundances from Sylvester and Eggins, 1997) but renormalized by a factor of 0.78 to bring these into consistency with the systematic offset noted for most other elements between NIST SRM 612 and the MPI-DING glasses.

Background-subtracted intensity ratios were then converted to elemental ratios (normalized to SiO₂) by multiplying by the RSFs. For the CAIs, major elements were calculated from oxide ratios of Si, Ti, Al, Mg, and Ca normalized to 100%, neglecting minor Na, Fe, Cr, etc., and the effect of Ti³⁺. For other elements, the concentrations were calculated from the elemental ratio multiplied by the SiO₂

content obtained from the major element procedure. Detection limits were calculated from three standard deviations of the blank intensities measured in the same analytical session. Where the concentration of a trace element was below the detection limit, the detection limit was substituted instead.

To judge the precision and accuracy of the technique, Table 3 shows analyses of Hf, Ta, W, Pt, and Au in six MPI-DING glasses calibrated against SRM 612. Each glass fragment (a few mm wide) was measured in three spots taken as far apart as possible using a 40 μm spot size, 10 Hz repetition rate, and 30 s dwell time per spot. All trace element data were standardized against NIST SRM 612, renormalized by a factor of 0.78, and using SiO₂ data for the MPI-DING glasses (Jochum et al., 2000). The measured Hf and Ta concentrations and those given as “reference values” by Jochum et al. (2006) agree to within ~5%. The W, Pt, and Au data in Jochum et al. (2000) are “information values”, and the Pt and Au concentrations are further listed

Table 3

Abundances of Hf, Ta, W, Pt, and Au in six MPI-DING glass standards (errors apply to the last place of decimal) determined by LA-ICP-MS using NIST SRM 612 as a standard (renormalized by 0.78)

	Hf		Ta		W		Pt		Au	
	($\mu\text{g/g}$)	Lit.	($\mu\text{g/g}$)	Lit.	($\mu\text{g/g}$)	Lit.	($\mu\text{g/g}$)	Lit.	(ng/g)	Lit.
GOR128-G	0.35 ± 1	0.35 ± 2	0.016 ± 1	0.019 ± 1	12.5 ± 2	15.5	8.6 ± 3	11.1	22 ± 2	24
KL2-G	3.99 ± 1	3.93 ± 14	0.93 ± 1	0.96 ± 2	0.38 ± 2	0.4	7.3 ± 2	16	83 ± 15	400
ML3B-G	3.22 ± 4	3.22 ± 8	0.53 ± 2	0.56 ± 1	0.29 ± 2	0.35	7.3 ± 2	8.8	64 ± 4	65
T1-G	4.11 ± 6	3.88 ± 15	0.49 ± 1	0.46 ± 2	0.54 ± 2	0.69	4.0 ± 4	6	75 ± 14	100
StHs6/80-G	3.32 ± 4	3.07 ± 9	0.42 ± 1	0.42 ± 2	0.30 ± 7	0.47	1.3 ± 5	1	39 ± 6	48
ATHO-G	14.6 ± 6	13.7 ± 5	3.9 ± 1	3.9 ± 2	7.5 ± 3	9.3	0.10 ± 1	8	22 ± 4	30

The literature values (Lit.) are from Jochum et al. (2006).

as possibly heterogeneous due to noble metal contamination in the glass preparation. Our data indicate relatively homogeneous values for Pt and Au at the LA-ICP-MS sampling scale. Our Au data (except for that of KL2-G) are relatively consistent with Au values determined by LA-ICP-MS reported in Jochum et al. (2006). The sensitivity and precision of our technique compares favorably with the bulk measurement techniques used in Jochum et al. (2000, 2006) for Hf and Ta, but the LA-ICP-MS technique used here is significantly more sensitive for W, Pt, and Au.

LA-ICP-MS analyses of EM2, the $\sim 300 \mu\text{m}$ metal particle in Ef2 described by Fisenko et al. (1992), were performed using both a line scan and a series of spot analyses performed subsequently along the track left by the line scan. A separate analytical method was used in which the peaks ^{27}Al , ^{29}Si , ^{31}P , ^{34}S , ^{45}Sc , ^{49}Ti , ^{51}V , ^{53}Cr , ^{57}Fe , ^{59}Co , ^{60}Ni , ^{89}Y , ^{90}Zr , ^{91}Zr , ^{92}Mo , ^{93}Nb , ^{94}Mo , ^{95}Mo , ^{179}Hf , ^{180}Hf , ^{181}Ta , ^{182}W , ^{193}Ir , ^{195}Pt , and ^{197}Au were acquired in low resolution ($R = 300$) at 50 ms/peak. The laser was operated at 10 Hz, 50% power output. A spot-size of $65 \mu\text{m}$ scanned at $10 \mu\text{m/s}$ was used for the line scan, and a spot-size of $40 \mu\text{m}$ with a dwell time of 20 s per spot was used for the spot analyses. The RSFs normalized to Fe were obtained from NIST SRM 1263a (Cr–V steel), NIST SRM 612, and the iron meteorites Hoba (IVB) and North Chile (Filomena, IIA) (Campbell et al., 2002; Campbell and Humayun, 2005) and are given, together with the elemental concentrations for the standards, in Table 2. Data reduction procedures were similar to those described above, and followed the general metal protocol used in previous papers (Campbell et al., 2002; Campbell and Humayun, 2005) with the exceptions noted below. NIST SRM 1263a is a Cr–V steel doped with Al, Ti, Zr, Nb, Mo, Hf, Ta, W, etc. Humayun and Campbell (2003) observed that Ti, Zr, Nb, Hf, and Ta were not homogeneously distributed in this standard on the microanalytical scale so that RSFs were obtained by rastering an $\sim 1 \text{ mm}^2$ area with a $100 \mu\text{m}$ beam rastered at $20 \mu\text{m/s}$. RSFs for the other standards were obtained using an $80 \mu\text{m}$ beam scanned at $10 \mu\text{m/s}$ along a 1.5 mm line scan. To check the fidelity of RSFs obtained from NIST SRM 1263a, a set of RSFs were calculated from the NIST SRM 612 silicate glass. Since the Fe abundance in SRM 612 is low (56 ppm), the intensity of the ^{57}Fe peak (e.g., 6 Kcps after background subtraction of 8 Kcps) was significantly lower than that obtained on metal standards (40–100 Mcps) so that direct Fe normalization

was not accurate. Accordingly, we normalized all the intensities for SRM 612 to ^{59}Co (200 Kcps), and then converted Co-normalized RSFs into Fe-normalized RSFs using the Co/Fe ratio in the metal standards (Table 2). Agreement between the RSFs obtained on a steel matrix and those obtained on a silicate glass matrix is excellent (Table 2) for many elements.

3. RESULTS

3.1. Efremovka Ef2

A reflected light image of the part of Ef2 containing the large metallic particle EM2 is shown in Fig. 1. The positions of three line scans, Ef12–14, Ef16–17, and Ef19–21, taken across Ef2 are shown. All three line scans were started on the end furthest from EM2 and concluded on the end nearest EM2, with two of the line scans terminating against EM2. All three line scans used a $25 \mu\text{m}$ beam diameter with a scan speed of $5 \mu\text{m/s}$, 10 Hz repetition rate and 50% power output. A single large fassaite grain was the target of Ef12–14 and Ef19–21. The large melilite immediately below EM2 in Fig. 1 was the target of Ef16–17. Abundant spinel inclusions are present, particularly in the melilite along Ef12–14 and Ef19–21, but are not visible in the reflected light image. However, a backscattered electron image of Ef2 in Campbell et al. (2003) shows the spinels clearly. Representative analyses of fassaite, melilite, metal (other than EM2) and spinel are given in Table 4. Since most of the spinel inclusions in CAIs are smaller than the beam diameter, there were few clean spinel analyses. A large spinel clump analyzed in Ef19–21 near EM2 provided the best analysis judged by the SiO_2 and CaO abundances. Typical of spinels in CAIs, we found that spinels in Ef2 are nearly pure MgAl_2O_4 with minor Cr (~ 2000 ppm) but no Ni. The elevated Cr abundances seen in some of the fassaite and melilite analyses (e.g., Melilite3 in Table 4) are due to spinel inclusions.

Profiles of Hf, W, and Pt abundances along the Ef19–21 line scan are shown in Fig. 2 on a log scale along with an image of the analyzed portion of the sample. The large fassaite grain (Fassaite1 in Table 4) has high Hf in the core (~ 14 ppm) decreasing towards the rim (< 3 ppm) with an average of around 11 ppm. A small fassaite grain encountered near EM2 has about 7 ppm Hf in its core. Between this fassaite and EM2, a spinel grain provided the spinel

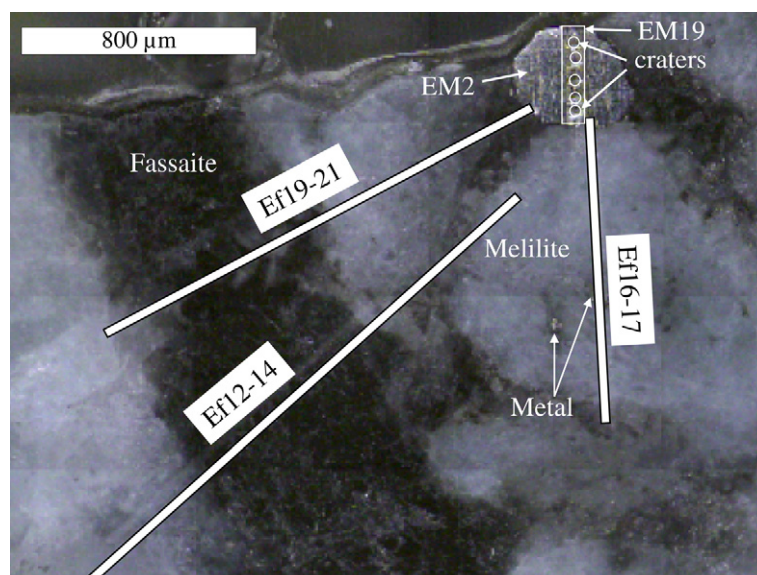


Fig. 1. Reflected light image of the part of Efremovka inclusion Ef2 that contains the large metal inclusion EM2 (marked). Locations of line scans are also marked. Vertical line scan (EM19) across EM2 is shown as a box, with the craters of five spot analyses taken after the line scan marked.

Table 4
Representative chemical analyses from Efremovka Ef2

Distance	Melilite1 7–52	Melilite2 65–193	Melilite3 7–867	Fassaite1 142–553	Fassaite2 940	Metal1 379–386	Spinel 1306
SiO ₂ (%)	33.9	26.69	26.97	38.1	34.13		3.00
TiO ₂	0.24	0.05	0.08	8.93	14.14		0.56
Al ₂ O ₃	16.1	28.39	26.86	17.8	18.26		65.70
MgO	8.8	3.97	4.63	9.8	7.84		23.40
CaO	40.9	40.91	41.46	25.3	25.63		7.30
Fe	0.00	0.00	1.85	0.01	0.01	52.88	0.17
Cr (ppm)	9	13	270	346	287	1823	1883
Ni	40	30	14000	127	27	467,600	40
Hf	0.10	0.006	0.07	11.3	25.1	0.16	0.21
Ta	0.142	0.031	0.18	0.62	0.57	2.7	0.46
W	0.13	0.042	18	0.45	0.008	437	0.20
Ir	0.02	0.013	22	1.7	0.003	750	0.03
Pt	0.31	0.190	18	1.7	0.248	590	0.09
Au	0.22	0.05	0.1	2.8	0.049	0.07	0.07
(W/Ir) _{Cl}	30	17	4.3	1.4		3.0	30
(Pt/Ir) _{Cl}	6.7	7.3	0.40	0.5	40	0.38	1
(W/Pt) _{Cl}	4.48	2.36	11	2.8	0.03	7.92	24
¹⁸⁰ Hf/ ¹⁸⁴ W	0.95	0.18	0.005	30	3706	0.0004	1.3

The distance (in μm) shows the length of a traverse averaged to obtain the listed composition. Italicized values are detection limits.

Notes. Melilite1, melilite to the left of fassaite along Ef19–21; Melilite2, average composition of melilite along Ef16–17 from start of traverse to the metal inclusion; Melilite3, average composition of melilite along Ef16–17 including the metal inclusion; Fassaite1, average composition of fassaite grain traversed by Ef19–21 (high Au caused by 3 large spikes over a background of 0.07 ppm); Fassaite2, single fassaite analysis from Ef12–14; Spinel, cleanest single analysis available along Ef19–21; Metal1, average of two analyses with highest Fe and Ni contents of metal inclusion along Ef16–17.

analysis shown in Table 4. Note that spinel has <1 ppm Hf. The Hf concentration in melilite is mainly below the detection limit (0.003 ppm). Hf appears to rise to ~1 ppm in some metallic inclusions encountered just prior to EM2, but the proximity of the fassaite surrounding EM2 along Ef19–21 makes interpretation of this as Hf in the metallic alloys unlikely. Both Pt and W vary from their detection

limits (<0.01 ppm) to values >10 ppm along the line scan in Fig. 2, from which we infer that neither element is present in the lattices of fassaite, melilite, or spinel, but appear to be entirely in metallic inclusions. These inclusions are ubiquitously present in all other mineral phases. The W/Pt ratio is variable, and transient spiking of W or Pt due to the laser encountering tiny metal inclusions causes some

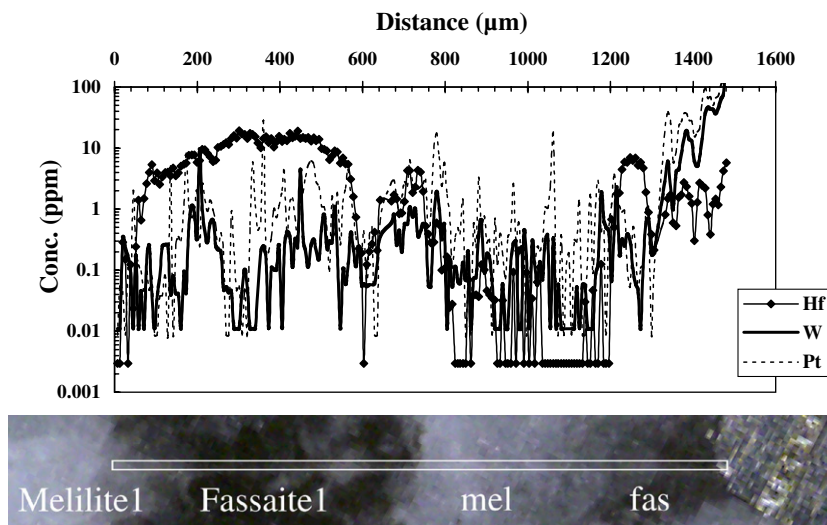


Fig. 2. Profiles of Hf, W, and Pt in line scan Ef19–21 taken across Ef2. The line scan begins in melilite (Melilite1), crosses the large fassaite grain (Fassaite1), and then passes through a melilite grain (mel) with numerous spinel inclusions (not visible) before entering the small fassaite grain (fas) bordering EM2. The analyzed portion of the reflected light image in Fig. 1 is shown approximately to the same distance scale as the analyses.

of the variability. A large metallic inclusion, encountered about midway in line scan Ef16–17 seen in Fig. 1, provided the metal composition shown in Table 4. Note the high Ni content of the metal, which is typical of metal in Ef2 (Campbell et al., 2003); the presence of ~ 3 ppm Ta in the metal; the superchondritic W/Ir ratio; and the low Pt/Ir ratio of the metal. All these features are also seen in metal from EM2 described below.

A line scan (EM19) was taken across EM2 with a 65 μm beam at 10 $\mu\text{m/s}$ in the vertical direction seen in Fig. 1. The locations of five spot analyses (40 μm diameter) taken in the track of EM19 are also marked in Fig. 1. Selected results for the metal analyses are given in Table 5. Results for Sc, Ti, Y, Mo, Hf, Ta, and W along the line scan EM19 are shown in Fig. 3. Elemental abundances for V, Cr, Ni, Co, Ir, Pt, and Au in EM2 agree with those reported in Campbell et al. (2003), but abundances of Mo and W are significantly higher, here. Campbell et al. (2003) reported negative Mo and W anomalies on a CI-chondrite normalized basis in most metal measured in Ef2, including EM2. However, we found positive Mo and W anomalies relative to Ir in EM2, and generally $\text{W/Ir} > \text{CI}$ in Ef2. The abundances of Mo (2920 ppm) and W (594 ppm) in EM2 obtained here are about $1.5\times$ (2000 ppm) and $3\times$ (210 ppm) higher, respectively, than the bulk EM2 values given in Campbell et al. (2003). However, the Pt/Ir ratio obtained here (0.47) is similar to that obtained by Campbell et al. (2003). The discrepancy in the Mo and W measurements is attributable to a lack of suitable standards for Mo and W in metal in Campbell et al. (2003). At the time those analyses were performed, Mo and W abundances in metal were obtained from RSFs calculated from the SRM 612 silicate glass. However, the problems noted above with using Fe as the internal standardizing element in SRM 612 glass probably contributed to the discrepancy. Here, we used the North Chile (Filomena) iron meteorite for W

calibration but obtained consistent RSFs for NIST SRM 1263a steel and SRM 612 glass (Table 1). Note, however, that a discrepancy of 50% would have occurred if the RSFs from SRM 612 glass were normalized exclusively to Fe intensities.

Important features of the EM2 line scan (EM19) shown in Fig. 3 include uniform Ti, Mo, Ta, and W contents in the core of EM2. The Mo and W contents decrease toward the rim, a feature also noted by Campbell et al. (2003), while the Ti and Ta contents increase toward the rim. The lithophile elements Sc, Y, and Hf were below their detection limits in the interior of EM2, but increase at the end of the line scan possibly due to the laser encountering a hidden fassaite inclusion near the rim of EM2. This is seen again in Hf in spot analysis EM 27 taken near the same rim, but Sc and Y remained below detection limits (Table 5).

3.2. Allende GBS

A backscattered electron (BSE) image of the Allende inclusion Golfball is shown in Fig. 4, and the locations of the three line scans taken are marked on this image. Two of the line scans were made with a beam diameter of 25 μm moving at 5 $\mu\text{m/s}$, 10 Hz repetition rate and 50% power output (identical to analytical parameters for Ef2, above), while GB23–24, which crossed the palisade body, was made with a finer beam diameter of 12 μm moving at 4 $\mu\text{m/s}$, 10 Hz repetition rate and 50% power output. Selected analyses of melilite, fassaite and a vein cross-cutting fassaite are given in Table 6. Simon et al. (2005) focused their efforts on two other sections of Golfball, so details of GBS are presented here. The palisade body (PB) is the circular feature in the lower right hand portion of the BSE image (Fig. 4). Most of the fassaite and melilite grains outside the palisade body have abundant spinel inclusions. The number of spinel inclusions was so great that most of

Table 5
Abundances (ppm) in CAI metal EM2 in Ef2

	EM19 Line	Detection limit Line	EM23 Spot	EM24 Spot	EM25 Spot	EM26 Spot	EM27 Spot	Average Spot	Detection limit Spot
Al	334	<i>150</i>	<i>2200</i>	<i>2200</i>	<i>2200</i>	<i>2200</i>	<i>2200</i>	<i>2200</i>	<i>2200</i>
Si	873	<i>80</i>	<i>1100</i>	<i>1100</i>	<i>1100</i>	<i>1100</i>	<i>1100</i>	<i>1100</i>	<i>1100</i>
P	7340	<i>1</i>	180	5870	9310	3560	2580	4300	20
S	93	<i>7</i>	<i>95</i>	<i>95</i>	<i>95</i>	<i>95</i>	<i>95</i>	<i>95</i>	<i>95</i>
Sc	<i>1</i>	<i>1</i>	<i>11</i>	<i>11</i>	<i>11</i>	<i>11</i>	<i>11</i>	<i>11</i>	<i>11</i>
Ti	9	<i>1</i>	<i>13</i>	<i>13</i>	<i>13</i>	<i>13</i>	<i>13</i>	<i>13</i>	<i>13</i>
V	8820	<i>0.1</i>	9080	9430	9880	9130	9490	9400	<i>1</i>
Cr	1100	<i>2</i>	1070	1070	1200	1090	1220	1130	<i>34</i>
Fe	391000	<i>120</i>	428000	412000	388000	421000	416000	413000	<i>2000</i>
Co	17500	<i>35</i>	17100	18000	17700	17900	17500	17600	<i>500</i>
Ni	562000	<i>1</i>	534000	545000	559000	538000	546000	544000	<i>20</i>
Y	<i>0.2</i>	<i>0.2</i>	<i>2</i>	<i>2</i>	<i>2</i>	<i>2</i>	<i>2</i>	<i>2</i>	<i>2</i>
Mo	2920	<i>0.06</i>	2200	1680	4110	2230	1730	2390	<i>1</i>
Hf	0.07	<i>0.02</i>	<i>0.2</i>	<i>0.2</i>	<i>0.2</i>	<i>0.2</i>	2.10	0.61	<i>0.2</i>
Ta	2.7	<i>0.004</i>	2.96	3.17	3.20	2.94	2.79	3.01	<i>0.06</i>
W	594	<i>0.01</i>	506	393	874	499	416	538	<i>0.2</i>
Ir	1260	<i>0.006</i>	1410	1440	1300	1350	1350	1370	<i>0.1</i>
Pt	1230	<i>0.007</i>	1310	1390	1240	1300	1290	1310	<i>0.1</i>
Au	1.63	<i>0.003</i>	0.16	0.20	0.23	0.19	0.23	0.20	<i>0.04</i>
(W/Ir) _{CI}	2.45		1.86	1.42	3.49	1.92	1.60	2.06	
(Pt/Ir) _{CI}	0.474		0.451	0.469	0.463	0.468	0.464	0.465	
(W/Pt) _{CI}	5.17		4.12	3.03	7.54	4.10	3.45	4.45	
¹⁸⁰ Hf/ ¹⁸⁴ W	0.0001		<i>0.0005</i>	<i>0.0006</i>	<i>0.0003</i>	<i>0.0005</i>	0.006	0.0013	

Italicized values are detection limits.

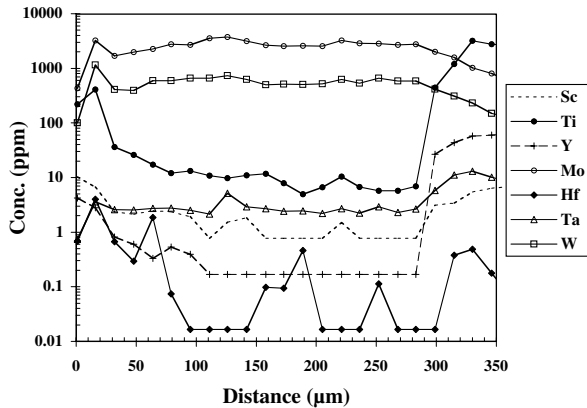


Fig. 3. Elemental abundance profiles of Sc, Ti, Y, Mo, Hf, Ta, and W across EM2. The flat portions of the profiles for Sc, Y, and Hf are below detection limits (see Table 5).

the fassaite analyses had to be corrected for spinel by normalizing the major elements to $\text{CaO} = 25.48\%$ (based on an average of 6 analyses in Simon et al., 2005). The extent of this correction was about 25% for the fassaite analyses from GB17–18 shown in Table 6; analyses with spinel content $>80\%$ were used to calculate the spinel end-member composition (not shown). In the palisade body, spinel inclusions were much sparser, so that fassaite3 in Table 6 did not need to be corrected for a spinel component. The spinel rim of the palisade body provided a set of the cleanest analyses available for spinel, which was found to be nearly pure MgAl_2O_4 with high Cr, like in Ef2. Due to beam overlap, the Cr contents in Allende GBS fassaite measured in this study correlated well with major element indicators of spinel, such as high Al_2O_3 or low CaO , and the fassaite Cr contents of ~ 400 – 450 ppm are derived from the high- CaO end of the correlation.

Profiles of Hf, W, and Pt across the palisade body (line scan GB23–24) are shown in Fig. 5 on a BSE image of

the line scan location at approximately the same scale. The BSE image shows the spinel-rich melilite (mel2: Melilite2, note high Cr) and fassaite to the left, outside the palisade body, and the spinel-free fassaite (e.g., fas3: Fassaite3) and melilite (mel3: Melilite3) to the right, inside the palisade body. Abundant OAs are present mainly in melilite, including one grain at the termination of GB23–24. A bright white line crossing the large fassaite grain along GB23–24 appears to be a tungsten-rich vein (vein1) with >100 ppm W (Table 6), but it is too narrow (<1 μm) compared with the laser beam size (12 μm) for a precise determination of its composition. The vein has <0.02 ppm Pt, the detection limit, and a $(\text{W}/\text{Ni})_{\text{CI}} \sim 3000$, but no detectable S (<3 ppm) (not shown). In general, both S (<3 ppm) and Au (<0.05 ppm) are below their detection limits in GB23–24, except at the terminal opaque assemblage. Inside the palisade body, both Pt and W are very low in the fassaite (Fassaite3), while outside the palisade body numerous Pt-rich inclusions are evident from the Pt spikes in Fig. 5. There was a series of spikes in Pt in the spinel boundary defining the palisade body, from which it is inferred that metallic and spinel inclusions are both concentrated at the margins of the body. The W/Pt ratio in the spinel-rich boundary and in the Pt spikes was subchondritic, with $\text{W} < 0.01$ (the detection limit). Although regions of high spinel abundance also had Pt spikes, from the lack of spatial correlation of Pt and Al_2O_3 spikes there is no reason to believe that Pt is bound in the spinel lattice, rather than that both spinel and Pt inclusions are concentrated into the same general region. The positions of fassaite grains can be easily distinguished by the Hf profile in Fig. 5, and fassaite can be seen to be zoned with respect to Hf, with high contents in the crystal cores, decreasing towards the rims. The core of the fassaite grain outside the palisade body has ~ 7 ppm Hf, while the large grain inside the body has ~ 15 ppm Hf in its core. Melilite has Hf close to or below the detection limit (0.01 ppm), and spinel inclusions in

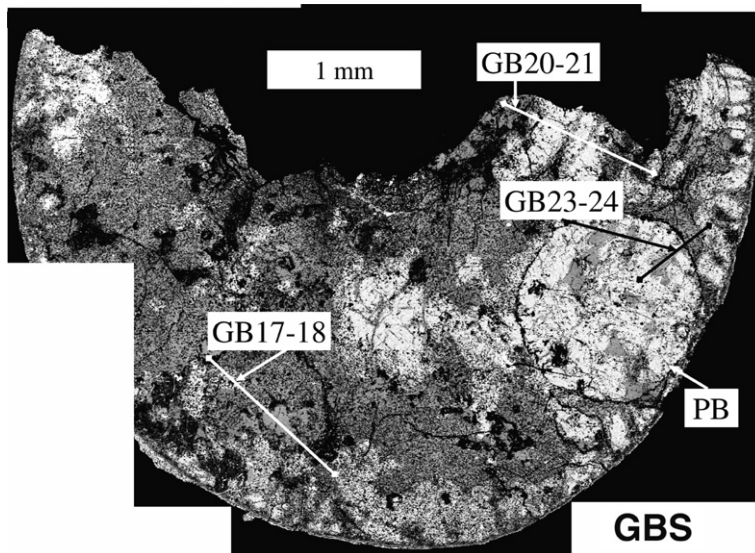


Fig. 4. Backscattered electron image of Allende inclusion GBS with location of line scans marked. The palisade body (PB) is at right.

Table 6
Representative chemical analyses from Allende GBS

Distance	Melilite1 488–1071	Melilite2 6–206	Melilite3 654–695	Fassaite1 212–424	Fassaite2 482	Fassaite3 437–514	Vein1 561
SiO ₂ (%)	34.10	31.65	31.72	40.06	38.64	36.60	34.32
TiO ₂	0.06	0.11	0.14	1.80	8.54	8.22	5.87
Al ₂ O ₃	16.90	25.08	19.81	20.53	17.63	20.15	19.11
MgO	9.22	11.32	7.40	12.39	10.01	9.07	10.26
CaO	39.73	31.85	40.93	25.48	25.48	25.94	30.45
Fe	0.20	0.29	1.88	1.36	0.06	0.06	3.61
Cr (ppm)	58	238	81	400	450	634	736
Ni	47	298	1476	2900	29	25	5330
Hf	0.01	0.015	0.147	1.97	9.67	13.32	8
Ta	0.045	0.032	0.161	0.91	0.48	0.426	0.19
W	0.11	0.68	4.68	4.35	0.006	0.14	136
Pt	0.10	3.51	0.10	120	0.007	0.03	0.02
Au	0.03	0.082	0.069	3.15	0.017	0.056	0.05
(W/Pt) _{CI}	11	2.07	511	0.39		50	>75,000
¹⁸⁰ Hf/ ¹⁸⁴ W	0.11	0.03	0.04	0.53	1839	109	0.07

The distance (in μm) shows the length of a traverse averaged to obtain the listed composition. Italicized values are detection limits.

Notes. Melilite1, average melilite composition from GB20–21 (GBS core); Melilite2, average melilite composition (with numerous spinel inclusions) from traverse GB23–24 taken outside the Palisade body (GBS mantle); Melilite3, average melilite composition from traverse GB23–24 taken inside the Palisade body near metal inclusion; Fassaite1; spinel-corrected (27%) average fassaite composition from GB20–21 (GBS core); Fassaite2, single analysis of mantle fassaite from GB17–18 corrected for 24% spinel; Fassaite3, average fassaite composition from short section of GB23–24 traverse relatively free of metal inclusions; Vein1, single analysis of fassaite + vein from GB23–24.

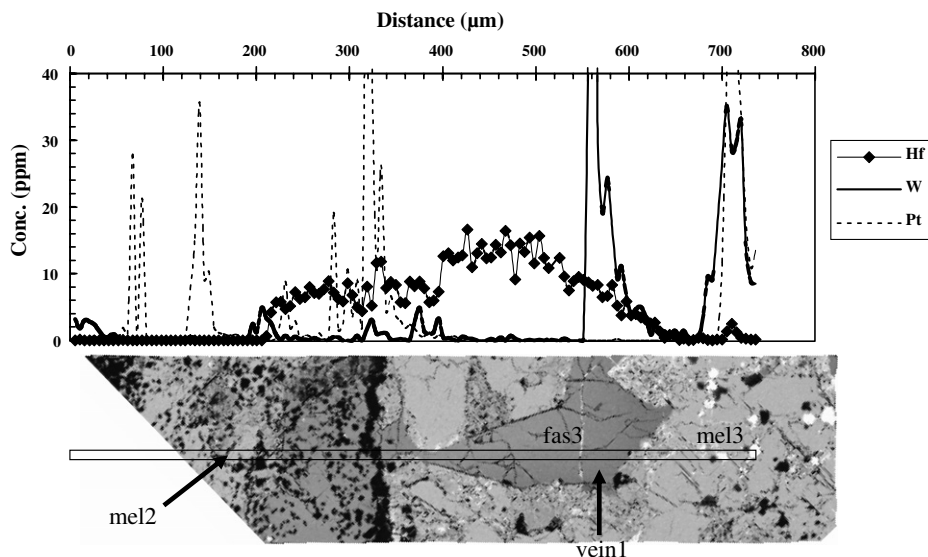


Fig. 5. Profiles of Hf, W, and Pt in line scan GB23–24 taken across the palisade body in Allende GBS. A portion of the BSE image of GBS is shown at approximately the same scale as the analytical profile with the position of the line scan marked. Fassaite, gray; melilite, light gray; spinel, black; metal, white. Note numerous spikes in Pt contents with W below detection (<0.01 ppm) outside the palisade body, and large W spike (135 ppm) with Pt below detection limit (0.02 ppm) in the vein cross-cutting fassaite. The final Pt–W spike is associated with a small opaque assemblage (OA). Note that fassaites inside the palisade body (e.g., fas3) are free of spinel inclusions (black specks), while those outside of the palisade body are filled with spinel inclusions. Locations of analyses given in Table 6 are marked: mel2 (Melilite2), mel3 (Melilite3), fas3 (Fassaite3), and Vein1.

melilite do not appear to contribute any Hf. In this regard, the mineral compositions in GBS are similar to those from Ef2, even though Ef2 fassaite (compact Type A) has higher Hf contents than that in GBS (Type B).

A line scan across a melilite-rich portion of the GBS section (GB20–21) from the core of Golfball towards its rim

yielded an average melilite composition (Melilite1 in Table 6) that has Ni, Hf, W, Pt, and Au near their detection limits. Likewise, Ti, Cr, Fe, and Ni are low indicating little or no contamination by fassaite (Ti, Hf), spinel (Cr) or opaque assemblages (Fe, Ni, W, and Pt). Fassaite1 in Table 6 comes from the upper end of GB20–21 (Fig. 4) and is low

in TiO_2 and Hf, but high in spinel (for which the composition shown was corrected) and in opaque assemblage components, contributing Ni, W, Pt, and even Au. The third line scan (GB17–18) was taken across a large mantle fassaite grain with numerous spinel inclusions (Fig. 4). Fassaite2 represents a single analysis from this line scan that was chosen for its remarkably low siderophile element content, having Ni, W, Pt, and Au all below their detection limits, demonstrating that these elements are not intrinsic to the fassaite grains.

4. DISCUSSION

4.1. Primary hosts of W and Hf

Since the mineral phases of Efremovka retain much of their primary composition, we will use elemental distributions in Efremovka Ef2 as a guide to primary CAI composition prior to modification by parent body processes. We will then examine Allende for primary features and later discuss the effect of parent body processes in both inclusions. There are two considerations that have to be weighed here: (1) intrinsic elemental compositions of the CAI mineral phases that are controlled by ionic radius, ionic charge, or other thermodynamic considerations; and (2) the apparent elemental compositions that would be measurable after mineral separations have been performed. The latter consideration is of interest from the perspective of ^{182}Hf – ^{182}W chronology, discussed later.

The exclusive host of W in Efremovka CAIs is Fe–Ni metal alloy. As already observed by Campbell et al. (2003), the abundances of W, Ir, and Pt are exceptionally high in EM2 (Table 5) for chondritic metal, about 2–3 orders of magnitude higher than in metal from ordinary chondrites (Humayun and Campbell, 2002; Campbell and Humayun, 2003), or from carbonaceous chondrites (Campbell et al., 2001, 2002, 2005; Campbell and Humayun, 2004). This is the result of refractory element enrichment in CAIs, although the level of enrichment in $(\text{W}/\text{Ni})_{\text{CI}} \sim 126$ in EM2 is higher than the enrichment factor of ~ 20 that characterizes refractory trace element enrichment (e.g., Hf and W) in bulk coarse-grained Allende CAIs (Grossman and Ganapathy, 1976). A few minor metal nuggets intersected along the line scans, e.g., in Ef16–17, also have high W, Ir, and Pt contents, in approximately the same relative proportions as EM2 (e.g., Metall in Table 4). The presence of numerous metal inclusions in CAI silicates, not clearly discerned in reflected light images, is inferred from the ubiquitous spikes of W, Ir, and Pt. Where Ir and Pt are below their detection limits, W is also below its detection limit (<0.003 ppm) in both melilite and fassaite. Spinel inclusions are usually too small to directly ascertain their intrinsic W abundances but the analyses with $\text{Al}_2\text{O}_3 > 60\%$ show no consistent W greater than detection limits. We conclude that W is below detection in melilite, fassaite and spinel, and that Fe–Ni metal alloy is its exclusive host. Further, excluding the large EM2 and Metall, the alloy appears to be distributed as numerous tiny nuggets particularly concentrated where spinel inclusions are concentrated.

The approximate dimensions of the Pt nuggets in CAI minerals other than metal can be inferred from the apparent concentration, by assuming that they either have ~ 1000 ppm Pt (e.g., EM2) or are essentially pure Pt, and knowing the volume analyzed. We assume that the analytical volume can be approximated by a hemisphere of 25 μm diameter (the beam diameter), yielding a volume of about 4 pL, or a mass of about 12 ng. An apparent Pt concentration of 1 ppm is then caused by a particle of about 1 μm radius with Pt ~ 1000 ppm, or of about 0.1 μm radius with Pt $\sim 10^6$ ppm. The latter corresponds closely to the dimensions of refractory metal nuggets observed in CAIs (0.1–0.05 μm) by TEM (Eisenhour and Buseck, 1992), although our data are consistent with a range of possible dimensions between 0.1 and 1 μm .

Fassaite is the exclusive host of Hf, where it is present at levels of ~ 20 ppm or lower in Ef2 and ~ 15 ppm or lower in GBS. By comparison, Palme et al. (1994) obtained 9.9–18.2 ppm Hf by INAA in a pyroxene-rich mineral separate from inclusion Egg-6 in Allende. Fassaite in both Ef2 and GBS are zoned, with decreasing Hf contents from the cores to the rims. Fig. 6(a) shows Hf plotted against CaO as a discriminant for fassaite from melilite and spinel. The typical values for CaO in fassaite (~ 25.5) and melilite (~ 40 – 41) are shown as gray lines on Fig. 6(a) based on values in Simon et al. (2005). Pure fassaite in both Ef2 and GBS form a vertical band around 25% CaO, with many analyses scat-

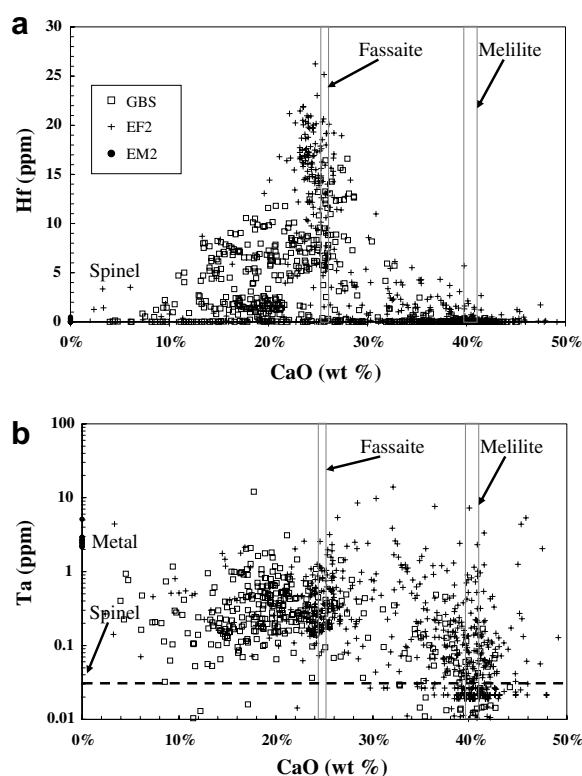


Fig. 6. A plot of (a) CaO vs. Hf and (b) CaO vs. Ta. The CaO ranges for fassaite, melilite, and spinel are shown for reference. Metal was assumed to contain no CaO. Note the high Ta content of EM2 metal (2–3 ppm). The detection limit for Ta (<0.03 ppm) is shown as the dashed line.

tering to lower CaO values because of the ubiquitous spinel inclusions. If spinel was an important host of Hf one would expect an inverse correlation with decreasing CaO (assuming spinel has $\text{CaO} < 0.1\%$). This is not observed in Fig. 6(a), where only four spinel analyses from Ef12–14 exhibit Hf between 1 and 4 ppm. These analyses were from a clump of spinels in the large fassaite in Fig. 1, and beam overlap on fassaite was the obvious source of the measured Hf as judged from the CaO contents of 2–6%. By comparison, Fisenko et al. (1992) found $\text{CaO} < 0.6\%$ in spinel from Ef2. These analyses can be contrasted with Allende spinel analyses from GB20–21 with $\text{CaO} \sim 2\text{--}6\%$ (from beam overlap with melilite) that have < 0.1 ppm Hf (Fig. 6a), including four analyses with Hf < 0.004 ppm (detection limit). The melilite analyses from both Ef2 and GBS have < 0.1 ppm Hf, with many analyses at the Hf detection limit, as seen in Fig. 2. There are evidently some mixed analyses of melilite + fassaite in the 1100 analyses shown in Fig. 6(a), and many more melilite + spinel mixtures that plot along the x -axis.

In both Ef2 and GBS, fassaite Hf contents are correlated with TiO_2 (total Ti-oxide) as shown in Fig. 7. The cores of the fassaites have Hf/ TiO_2 higher than the chondritic ratio (black line in Fig. 7), which decreases towards the rim, becoming subchondritic. Also plotted on Fig. 7 are ion microprobe analyses of Hf and TiO_2 in Allende fassaites from Type B CAIs (Simon et al., 1991), and bulk INAA data for Hf and TiO_2 abundances in refractory inclusions from CV chondrites (Sylvester et al., 1992, 1993). The 20 bulk CAI analyses plot along the CI chondrite line with three exceptions. The individual Allende Type B fassaite data from Simon et al. (1991) plot nearly identically with those of GBS (which was not included in that study), but do not show the suprachondritic Hf/ TiO_2 ratios.

Humayun et al. (2006) noted that there were small Hf spikes (Hf ~ 0.1 ppm) associated with metal inclusions in both GBS and Ef2. Although beam overlap with fassaite may have contributed to the Hf, these spikes were also observed in metal (high Ni, W, Pt) inclusions in melilite (e.g.,

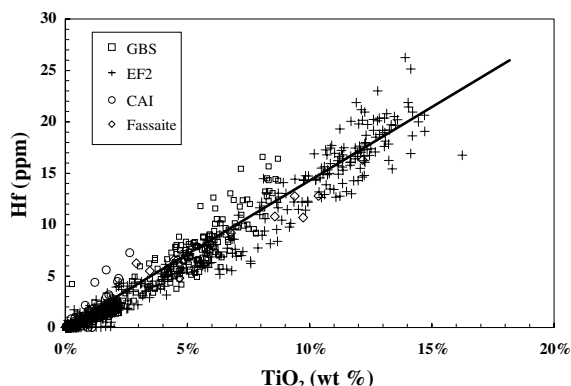


Fig. 7. Correlation of Hf with TiO_2 in Allende GBS (squares) and Efremovka Ef2 (crosses) silicates. The line represents the CI chondritic ratio (from Anders and Grevesse, 1989) for the two elements. Also shown are Allende fassaite analyses (diamonds) from Simon et al. (1991) and bulk CAI data (circles) from Sylvester et al. (1992, 1993).

Fig. 2), leading Humayun et al. (2006) to suggest that Hf might be present in metal. Subsequent re-examination of the Hf spikes in metal inclusions associated with melilite revealed a different explanation: residual isobaric interference from ^{180}W . Since the ^{180}Hf isotope was monitored for Hf abundance, a correction for ^{180}W had to be applied using ^{182}W as the reference isotope and assuming a constant $^{180}\text{W}/^{182}\text{W} = 0.0045$. However, since the $^{182}\text{W}+$ (and $^{183}\text{W}+$) signals can experience sharp transients (< 0.050 ms) from small particles, the fidelity with which the ^{180}W can be interference-corrected by reference to ^{182}W is diminished in the presence of $^{182}\text{W}+$ signals that fluctuate between measurements of successive peaks. This had not been taken into account by Humayun et al. (2006). We noted that negative residuals of 0.1 ppm were not uncommon in sections with high W signal and reasoned accordingly that similar positive residuals must also remain in our data. In the absence of an obvious means to quantify the effects of transients, we cannot assign a number to the higher Hf detection limits achieved in the presence of high W signals but estimate < 0.2 ppm Hf from the inversion of the negative residuals.

We have investigated the presence of Hf in metal further by analyzing the large metal particle EM2 in Ef2 by laser ablation while monitoring both ^{179}Hf and ^{180}Hf . As can be seen from the Hf profile for EM2 (Fig. 3), Hf is mostly below detection limits (0.02 ppm). The high Hf encountered at the beginning of the line scan is mainly controlled by residual signal from the CAI rim adjacent to EM2 where the analyses were initiated. To overcome this problem, a set of five spot analyses (40 μm) were taken in the same track which yielded Hf < 0.2 ppm (detection limit), except in the final spot (EM27 in Table 5). Although EM27 may have encountered fassaite underneath the metal (as discussed earlier), the amount of Hf present is negligible as seen from the $^{180}\text{Hf}/^{184}\text{W}$ ratio in Table 5. Accordingly, we conclude that Hf is not present in metal based on direct analyses.

4.2. Nominally lithophile elements in CAI metal

We term elements that are usually lithophile but might become siderophile under reducing conditions nominally lithophile elements. El Goresy et al. (1978) reported the occurrence of Zr, Nb, and Ta in Pt-rich metal nuggets from Allende, which were inferred to have formed under very reducing conditions. Fig. 3 shows the results of the EM19 traverse for Sc, Ti, Y, Mo, Hf, Ta, and W. Under the reducing conditions of the solar nebula, a substantial number of nominally lithophile elements (e.g., Ti, V, and Ta) can be observed to partition into the Fe–Ni metal (Table 5), and their distribution is reasonably homogeneous, similar to the distribution of W (Fig. 3). On finer spatial scales, V is heterogeneously distributed in the core of EM2 as V-magnetite and V-sulfide grains which were observed by X-ray mapping with an EDX detector (Fisenko et al., 1992; Campbell et al., 2003). The broad beam used in the EM19 line scan resulted in significant averaging of these exsolution products. While V was known from CAI metal (Fisenko et al., 1992; Campbell et al., 2003), the presence

of ~ 3 ppm Ta is a good indicator of the reducing conditions under which EM2 and Ef2 formed. In the spot analyses, Ti was below detection limit (13 ppm), but was resolved at ~ 9 ppm in the line scan. The trivalent elements Sc (< 1 ppm) and Y (< 0.2 ppm) were below detection limits. This selective elemental partitioning indicates that Ta has indeed become siderophile and that the presence of some nominally lithophile elements in EM2 metal seen in Fig. 3 is not due to the presence of trace silicate/oxide mineral inclusions, or beam overlap on surrounding mineral grains (with exceptions previously noted). The $^{180}\text{Hf}/^{184}\text{W}$ ratio for the EM19 line average composition is 10^{-4} (Table 5), which is much smaller than any reported $^{180}\text{Hf}/^{184}\text{W}$ value from Allende CAI magnetic separates (Kleine et al., 2005a). Radiogenic ingrowth of ^{182}W in CAI metal from Efremovka is precluded by these data.

4.3. Hosts of Ta and the Ta/W ratio

Fig. 6(b) shows the distribution of Ta vs. CaO. In Efremovka Ef2, Ta is concentrated in fassaite (0.1–1 ppm) and in metal, and is below detection (< 0.03 ppm) in many melilite analyses. Examination of the line scans (not shown) indicates that the frequent spikes of Ta in melilite (less so in fassaite) are also high-W regions which are by inference metal inclusions. The core of EM2 contains about 2 ppm Ta, with up to 10 ppm in the rim. This high-Ta part of EM2 also has high TiO_2 and Hf contents. Likewise, the metal hosted in melilite in Ef16–17 has ~ 3 ppm Ta (Table 4). Spinel contains little measurable Ta, but beam overlap with adjacent metal does not allow a firm upper limit to be inferred.

The Ta/W ratio in fassaite (not shown) ranges from ~ 10 to < 1 . The high Ta/W ratio in fassaite is important for considerations of thermal neutron capture on ^{181}Ta to form ^{182}W , since positive $\epsilon^{182}\text{W}$ anomalies can arise from cosmic-ray irradiation of silicates with high Ta/W ratios (Kleine et al., 2005b). Leya et al. (2000) showed that at a Ta/W ~ 0.22 , the thermal neutron capture on ^{181}Ta proceeded at the same rate as the burn-out of ^{182}W ; at Ta/W > 0.22 net production of ^{182}W occurs, while at Ta/W < 0.22 neutron capture burn-out of ^{182}W takes place. For comparison, the CI value of Ta/W = 0.15 (Anders and Grevesse, 1989). The ^{21}Ne cosmic-ray exposure age (T_{exp}) of Allende is 5.2 Ma (Scherer and Schultz, 2000), and the average cosmic-ray exposure age of CV chondrites is 13 ± 10 Ma (Herzog, 2006). For these values of T_{exp} , the equations given by Leya et al. (2000) indicate that significant impact on the $\epsilon^{182}\text{W}$ occurs at Ta/W > 50 , with a range of 0.7–5.3 ϵ units for Ta/W = 100, for deeply buried CAIs in the irradiated meteoroid. For such high values of Ta/W, the Hf/W ratio is also likely to be very high so that the neutron capture effects on ^{181}Ta impacting $\epsilon^{182}\text{W}$ are second-order corrections for fassaites from CAIs in CV chondrites.

4.4. Better mineral separates for ^{182}Hf – ^{182}W chronology

The selection of representative analyses shown in Tables 4 and 6 were chosen on the basis of two distinct criteria: (1) intrinsic contents in CAI minerals; and (2) representative averages that show the effects of metal inclusions on the

compositions of melilite or fassaite grains that could be hand-picked from crushed CAI chips. For example, Fassaite1 in Table 4 is an average composition of an ~ 400 μm -long line scan of the large fassaite grain shown in Fig. 1. It has 0.45 ppm W and a low $^{180}\text{Hf}/^{184}\text{W} = 30$ compared with Fassaite2 from the same grain (a single analysis picked for its low siderophile element content) which has $^{180}\text{Hf}/^{184}\text{W} > 3700$ (because W is below the detection limit). However, Fassaite1 may be more representative of the composition of a hand-picked pyroxene separate from a crushed CAI chip. Likewise, Melilite3 represents an average over the entire melilite grain (~ 1 mm) traversed by Ef16–17, with 18 ppm W and $^{180}\text{Hf}/^{184}\text{W} = 0.005$. The high siderophile element content is contributed by numerous metallic inclusions, including the large metal in Table 4. The positions of two of these inclusions are marked by arrows in Fig. 1. Similarly, in Allende GBS, Melilite1 is an average of ~ 0.5 mm of core melilite with $^{180}\text{Hf}/^{184}\text{W} = 0.11$, and Fassaite1 from the same line scan averages $^{180}\text{Hf}/^{184}\text{W} = 0.53$, which is very low for fassaite.

Fig. 8 is a plot of $^{180}\text{Hf}/^{184}\text{W}$ vs. CaO in all measured points from Efremovka Ef2 and Allende GBS. The CaO contents distinguish fassaite from melilite with representative ranges of CaO indicated by vertical lines as in Fig. 6. Spinel would plot with CaO $< 0.1\%$, and metal was plotted with CaO = 0%. The $^{180}\text{Hf}/^{184}\text{W}$ ratio in fassaite is clearly higher than that in melilite despite the 2–3 orders of magnitude range induced by numerous metallic inclusions present in both minerals. The $^{180}\text{Hf}/^{184}\text{W}$ ratio in fassaites is as large as 2000 in GBS and 3500 in Ef2, with the majority of fassaite analyses having $^{180}\text{Hf}/^{184}\text{W} > 20$. Most melilite analyses have $^{180}\text{Hf}/^{184}\text{W} < 20$ by comparison, with a typical range of 0.01–10. Thus, mineral separates of melilite and fassaite provide reasonably large differences in $^{180}\text{Hf}/^{184}\text{W}$ for purposes of ^{182}Hf – ^{182}W chronology. The presence of spinel inclusions (ubiquitous in fassaite) appear to move the data points horizontally towards lower CaO without

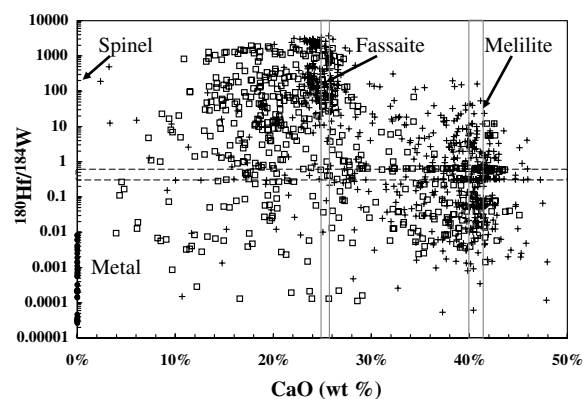


Fig. 8. The distribution of $^{180}\text{Hf}/^{184}\text{W}$ ratios in the mineral phases of CAIs; legend same as in Fig. 6. Approximate CaO contents of fassaite and melilite are shown as gray lines; CaO content of metal is assumed to be 0, while that of pure spinel is < 0.1 . Dashed box represents ratios of the detection limits of Hf and W in Ef2 and GBS. Note that fassaites have distinctly higher $^{180}\text{Hf}/^{184}\text{W}$ than melilites, and that the effect of spinel inclusions is to move the data points horizontally towards lower CaO.

apparently affecting the $^{180}\text{Hf}/^{184}\text{W}$ ratio. This is consistent with our discussion above where it was concluded that spinel does not appear to be a host for either Hf or W. Since both Hf and W are at or near their detection limits in melilite, the ratio of their detection limits is of interest here. The value in Ef2 is 0.3, and in GBS it is 0.5–0.64, which are marked in Fig. 8 by the dashed box. The density of data points within this box speaks to the number of melilite analyses that have both Hf and W below their detection limits. (Some analyses falling in this box at $\text{CaO} < 25\%$ are likely to be melilite + spinel mixtures, rather than fassaite analyses, since fassaite analyses do not have Hf near detection limits.) Melilite analyses with $^{180}\text{Hf}/^{184}\text{W} < 0.3$ have contributions from metal particles; those with $^{180}\text{Hf}/^{184}\text{W} > 1$ have beam overlap with fassaite. Thus, a fassaite-free separate of melilite should yield $^{180}\text{Hf}/^{184}\text{W} < 1$.

By comparison, Kleine et al. (2005a) obtained $^{180}\text{Hf}/^{184}\text{W} < 3$ in all their analyses. Their highest $^{180}\text{Hf}/^{184}\text{W}$ values were obtained on “fines” and their non-magnetic fraction, where the Hf abundance was ~ 2 ppm. A weakly magnetic fraction, tentatively identified as a “pyroxene” separate, had $^{180}\text{Hf}/^{184}\text{W} = 0.727$, comparable to that of the bulk CAI (A37, from Allende). Thus, the mineral separates prepared by Kleine et al. (2005a) did not achieve a significant enhancement of the Hf/W ratio relative to the bulk CAI value. We infer from their Hf abundances that the fractions labeled “fines” and “NM” had fassaite/bulk CAI ratios $< 2\times$ enhanced. The lower Hf abundance (0.949 ppm) in the fraction labeled “WM” indicates that this fraction contained less fassaite than some of the other fractions (2.2–2.5 ppm Hf) and could not have been a “pyroxene” separate. The variation in $^{180}\text{Hf}/^{184}\text{W}$ measured in EM2 metal (including potential effects of beam overlap with surrounding silicates) is 0.01–0.00003, with a mean $^{180}\text{Hf}/^{184}\text{W} = 0.00015$. We calculate that the difference in $\epsilon^{182}\text{W}$ due to radiogenic ingrowth is less than 2 ppm for this entire range of variation. The magnetic fraction recovered by Kleine et al. (2005a) from Allende CAI All-MS-1 is somewhat higher ($^{180}\text{Hf}/^{184}\text{W} = 0.0237$) but the difference between lowest and highest $^{180}\text{Hf}/^{184}\text{W}$ in their study is small compared with the range observed here. The more significant issue for the purposes of Kleine et al. (2005a) was not obtaining a sufficiently high enhancement of fassaite in their separates to obtain better control of their isochron at $^{180}\text{Hf}/^{184}\text{W}$ higher than bulk CAI values.

Another useful guide to determining whether a mineral separate has much fassaite in it is provided by the correlation of Hf with TiO_2 (Fig. 7). In the absence of perovskite, a quick check of any fassaite-dominated mineral separate by SEM-EDX could provide an approximate Hf abundance using the Hf– TiO_2 correlation.

4.5. Effects of parent body processes on ^{182}Hf – ^{182}W chronology

When refractory metal-rich particles were first described from Allende they were interpreted to have formed prior to the formation of the CAIs in which they were hosted, and were termed Fremdlinge by El Goresy et al. (1978). Subsequent investigations of the mineral composition and phase

assemblages of Allende “Fremdlinge” led Blum et al. (1989) to the conclusion that these objects were produced by alteration processes in the meteorite parent body from primary Fe–Ni metal alloys enriched in refractory elements, and they termed them opaque assemblages (OAs). Beckett et al. (1988) examined indicators of redox conditions in Allende CAIs and concluded that the Mo–W depletions and scheelite–powellite associations observed in Allende OAs were due to oxidizing conditions encountered on the parent body. Palme et al. (1994) studied OAs from the large Allende CAI Egg-6, and showed that W deficiencies observed in the OAs were complemented by W excesses in the silicates surrounding the OAs. They proposed that W was oxidized and combined with Ca to form scheelite–powellite solid solutions (see also Blum et al., 1989). Bischoff and Palme (1987) reported scheelite–powellite solid solutions from OAs in Allende CAI A37, an inclusion analyzed for ^{182}Hf – ^{182}W by Kleine et al. (2005a), but interpreted their origin in terms of nebular processes. Palme et al. (1994) inferred a multi-stage process for the origin of OAs, including condensation of refractory metal alloy, incorporation into CAIs, oxidation and sulfurization of OAs and “extensive redistribution of elements during alteration”. They convincingly showed that OAs must have been oxidized after incorporation into CAIs but considered that this must have occurred prior to the accretion of the Allende parent body because of the variable conditions of oxidation and sulfurization of OAs observed from different CAIs. The latter argument is less persuasive since variable alteration conditions may occur on the local scale at which OAs were formed in the Allende parent body. Comparison of refractory metal alloy in Efremovka and other reduced CV3 chondrites with the OAs in Allende (CV3 oxidized) indicates that the mineral assemblages found in OAs likely formed on the Allende parent body and last equilibrated at ~ 770 K (Blum et al., 1989). This is important from the perspective of the timing of alteration and W mobility, i.e., the $\epsilon^{182}\text{W}$ of the alteration products, since alteration on the Allende parent body may have occurred as late as 15 m.y. after the formation of CAIs (for a review of the chronology of alteration on Allende, see Krot et al., 2006).

To assess the mobility of W in CAIs, let us consider the LA-ICP-MS data from Efremovka Ef2 and Allende GBS. Under the reducing conditions in which Ef2 formed, where nominally lithophile elements such as V and Ta entered the metal phase, W is expected to behave entirely like a siderophile element. However, W would have become lithophile had mild oxidation of the inclusions occurred during metamorphism. Campbell et al. (2003) carefully documented the fact that even the rather pristine EM2 metal had undergone minor sulfidation (V, Mo-sulfides) and oxidation (V-magnetite). Further, they showed that W had been lost from the rim of EM2. Our new work shows that W has not significantly mobilized into the silicates of Ef2, and that there is no resolvable diffusion profile into either the melilite or the fassaite grains that border EM2 (Fig. 2). A plot of W vs. Pt (Fig. 9) shows that these elements are correlated in both Ef2 and GBS, though the correlations are not perfect in either inclusion. In EM2 metal, W and Pt are strongly correlated, and the W/Pt ratio is clearly superchondritic.

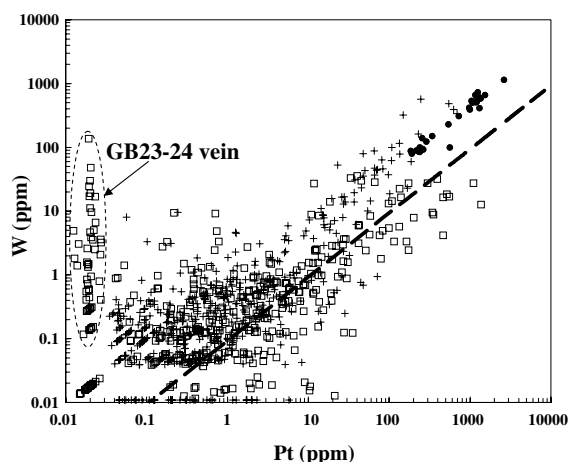


Fig. 9. Tungsten vs. platinum in all line scans from Allende GBS, Efremovka Ef2 and EM2; legend same as in Fig. 6. The line represents the CI chondrite value (Anders and Grevesse, 1989). Note high W (up to 100 ppm) in Allende GB23–24 (dashed ellipse) with Pt below detection limits (0.02 ppm). Also note that small Efremovka metal inclusions in Ef2 silicates have a similar superchondritic W/Pt ratio as EM2 while most Allende metal inclusions have a chondritic–subchondritic W/Pt ratio.

Metal grains in Ef2 encountered as inclusions in silicates exhibit the same high $(W/Pt)_{CI} \sim 3\text{--}5$. Metal inclusions in Allende GBS exhibit a subchondritic $(W/Pt)_{CI}$ ratio. The data for both Ef2 and GBS become noisy at low concentrations ($W < 1$ ppm), as expected, due to low ion counts (< 20 counts). An interesting feature is the array of GBS points with 0.1–100 ppm W that straddle the Pt detection limit (~ 0.02 ppm). These points all come from the single W-rich vein (vein1) cross-cutting fassaite seen in Fig. 5. It should be noted that this particular W peak is slightly asymmetric, rising sharply but declining more slowly (Fig. 5). Humayun et al. (2006) showed this same feature on a log scale and indicated that the entire portion of fassaite seen to the right of the vein in Fig. 5 may have been contaminated with “lithophile” W. In Fig. 5, the same data are shown on a linear scale and the asymmetry is attributable to the incomplete “wash-out” of the W signal. It is no longer clear that this is lithophile W in the fassaite. It is, however, clear that, in Allende, W has been oxidized, decoupling it from other siderophile elements like Pt, and mobilizing it in veins in the inclusion. It is also apparent that a vein with extremely high W concentrations is cross-cutting fassaite, the Hf carrier in CAIs ($^{180}\text{Hf}/^{184}\text{W} \sim 2000$) increasing the potential for isotopic exchange between the two phases during metamorphism.

Although the laser ablation technique has proven ideal for determining the distribution of Hf and W among mineral phases in CAIs, it cannot establish that isotopic redistribution has accompanied elemental redistribution by direct measurement. However, several lines of reasoning indicate that isotopic disturbance is highly plausible. The elemental composition of the vein portion of the fassaite (Table 6) shows high Ca (30% compared with 25% in fassaite), Fe (3.6%), Ni (5000 ppm), and W (135 ppm), but no S

(< 3 ppm), Pt (< 0.02 ppm) or Au (< 0.05 ppm). Other evidence that exogenous material infiltrates CAIs is provided by the correlation between Na and Au contents for CAIs, the highest of which occur in Allende CAIs (Sylvester et al., 1993). It is important to remember here that fluids required to provide the O, S, and Au, for the formation of OAs did not originate within the CAI, but must have permeated through fractures (now veins) from the matrix outside (see Krot et al., 2006; for a review of alteration conditions in Allende). If the oxidizing fluids carried Na, S, and Au in from the matrix, it is very likely that they also carried radiogenic W in from the matrix. Given that the W mass balance is controlled by Fe–Ni alloy, much of the W in OAs was probably derived from alteration of refractory metal but the prospect of having radiogenic W incorporated from the matrix implies that the isotopic composition of W in OAs (or magnetic separates) may not be the least radiogenic W in the solar system.

4.6. Isochron or mixing line?

The discussion above leads to the question of whether the linear array observed on a plot of $\epsilon^{182}\text{W}$ vs. $^{180}\text{Hf}/^{184}\text{W}$ reported by Kleine et al. (2005a) is an isochron or a mixing line. The case for an isochron can only be argued for a closed system. (The interested reader may wonder whether bulk CAIs can be treated as “whole rocks” for the purposes of ^{182}Hf – ^{182}W chronology, but their dimensions are not sufficiently large compared with the transport distances of W to treat these as effectively closed systems.) The arguments above indicate that the system may have been open with respect to W transport, and that the isochron reported for Allende CAIs may be a mixing line. Even though W transport was documented above, without *in situ* W isotope data the range of possibilities permit both an entirely endogenous origin of W, or a mixed endogenous and exogenous origin referred to here as “radiogenic W” even if the $\epsilon^{182}\text{W}$ is less than the carbonaceous chondrite value, $\epsilon^{182}\text{W} = -1.90$ (Kleine et al., 2002; Yin et al., 2002). We will, therefore, consider the answer to be model dependent and examine three possibilities below: (a) purely endogenous W, (b) mixing of endogenous and exogenous W, and (c) metamorphic equilibration of mixed W.

The first possibility (a) is that the W in Allende CAI veins was entirely endogenous, i.e., the fluids carried no W into the CAI but may have carried W out of the CAI. In this case, W derived from the alteration of refractory metal alloy was incorporated to different degrees in the various mineral separates and the slope of the mixing line is identical to that which would have been observed had all the W been of primary origin. This is the interpretation taken by Kleine et al. (2005a), who recognized that secondary formation of the OAs did not necessarily imply a rotation of the isochron, and they concluded that “we interpret the All-MS-1 isochron to date the formation of this CAI”.

The second possibility (b) is that radiogenic W was introduced into All-MS-1 and A37 from the Allende matrix, which increased the $\epsilon^{182}\text{W}$ of the “magnetic fraction” of the CAIs (from a primary $\epsilon^{182}\text{W}$ lower than ~ -3.5) without changing the $\epsilon^{182}\text{W}$ of the fassaite grains. The forma-

tion of scheelite–powellite solid solutions as observed in A37 by Bischoff and Palme (1987), and inferred to occur in other CAIs (e.g., GBS), requires that the oxidizing fluids must have added Ca, as well. If the source of this Ca was the CAI minerals then it must be argued that melilite (free of Hf and its ^{182}W decay product) was the sole phase to undergo secondary alteration for the scenario considered above (a) to still hold true. Alteration of fassaite (the carrier of Hf and ^{182}W) would liberate radiogenic W into the fluids. Additional mineral phases may have been involved if the source was the Allende matrix. Thus, the second, and less restrictive, possibility is that secondary W was distributed about the CAI in its OAs, and that the linear array of data points obtained by Kleine et al. (2005a) is a mixing line between a secondary W-rich phase and primary fassaite. In this case, the slope of the apparent isochron would be indistinguishable from that which would be obtained from primary CAI minerals alone (because the fixed point occurs at $^{180}\text{Hf}/^{184}\text{W} > 1000$), but the intercept would be displaced to higher $\epsilon^{182}\text{W}$ (Fig. 10). In Fig. 10, the thick line represents an isochron with the parameters of Kleine et al. (2005a), passing through their carbonaceous chondrite value (CC). The inset shows the data used by Kleine et al. (2005a) to calculate the slope of their isochron, including a bulk CAI analysis from Yin et al. (2002). The $^{180}\text{Hf}/^{184}\text{W}$ values of metal-free fassaites measured in GBS (>1839) and Ef2 (>3706) are indicated by vertical arrows in Fig. 10, and their corresponding $\epsilon^{182}\text{W}$ values are GBS ~ 2000 and Ef2 ~ 4000 on the Kleine et al. (2005a) isochron. In the inset, two mixing lines are shown between hypothetical clean fassaite and metal (or OAs) with assumed initial $\epsilon^{182}\text{W} = -4.0$ and $\epsilon^{182}\text{W} = -4.5$ (arbitrarily

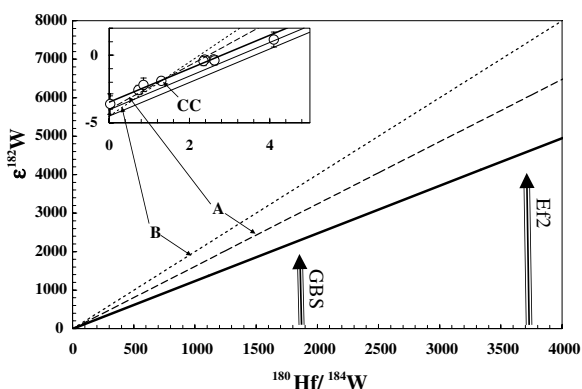


Fig. 10. $\epsilon^{182}\text{W}$ vs. $^{180}\text{Hf}/^{184}\text{W}$ plot showing analytical results of Kleine et al. (2005a) on two CAIs with their 2σ error bars. The thick black line is the isochron reported by Kleine et al. (2005a). The dashed lines (A and B) represent two model isochrons, each passing through the carbonaceous chondrite point (CC) in Kleine et al. (2005a) with different initial $\epsilon^{182}\text{W}$ values: A = -4.0 , and B = -4.5 . The *in situ* $^{180}\text{Hf}/^{184}\text{W}$ compositions measured in the cleanest fassaites from GBS and Ef2 are plotted as broad vertical arrows, since $\epsilon^{182}\text{W}$ is not available for them. The inset expands the region $^{180}\text{Hf}/^{184}\text{W} = 0\text{--}4$ where the data of Kleine et al. (2005a) plot. The two solid lines parallel to the isochron with intercepts at $\epsilon^{182}\text{W}$ values of -4.0 and -4.5 are model mixing lines (see text for discussion).

selected for the purposes of this argument). The exact location of the fassaite is not important, here; as long as its $^{180}\text{Hf}/^{184}\text{W}$ value is large (>1000) the mixing lines essentially parallel the isochron (Fig. 10). Such mixing lines do not pass through the CC value for $\epsilon^{182}\text{W} < -3.5$ in Fig. 10, which constitutes an argument against the second possibility.

The third possibility (c) is that radiogenic W in fassaite and unradiogenic W in veins or OAs bordering fassaite isotopically exchanged during metamorphic equilibration. Allende is weakly metamorphosed and is classified as a type 3.2 (Guimon et al., 1995). Alteration of Allende CAIs mobilized W into veins placing it in close proximity to fassaite (radiogenic ^{182}W host). During metamorphism, isotopic exchange can rotate the isochron about the CC value. This is illustrated in Fig. 10 by lines A and B, which are hypothetical isochrons calculated for assumed initial $\epsilon^{182}\text{W} = -4.0$ (A) and $\epsilon^{182}\text{W} = -4.5$ (B). Given that the metamorphism is weak, partial equilibration can be expected so that portions of large metal-free fassaites, and OAs in melilites, may retain their original $\epsilon^{182}\text{W}$. However, OAs adjacent to fassaite are most likely to exchange W isotopically. In such an instance, the “magnetic” fraction of a CAI could be biased to higher $\epsilon^{182}\text{W}$ by the presence of partially equilibrated OAs, and the isochron reported by Kleine et al. (2005a) would have a shallower slope than the original isochron. The initial $\epsilon^{182}\text{W}$ could then be less radiogenic than the value of -3.47 ± 0.20 reported by Kleine et al. (2005a) with important ramifications for the chronology of the early solar system. Because of partial equilibration, some fassaite grains could retain higher initial $\epsilon^{182}\text{W}$ values, e.g., GBS ~ 3500 and Ef2 ~ 7000 , for the model B isochron (Fig. 10). This indicates the value of *in situ* measurements of the $\epsilon^{182}\text{W}$ in fassaites even with lower precision than the measurements of Kleine et al. (2005a). The concentration of ^{182}Hf in fassaites (assuming $^{182}\text{Hf}/^{180}\text{Hf} = 1 \times 10^{-4}$) is about 10^{14} atoms/g. In the LA-ICP-MS method used in the present study, an isotope effect was not resolved in the $^{182}\text{W}/^{183}\text{W}$ ratio, since the highest values of $^{180}\text{Hf}/^{184}\text{W}$ obtained on fassaites represent lower limits where the ^{182}W was below its detection limit.

An alternative reason for iron meteorites to have lower $\epsilon^{182}\text{W}$ than CAIs is cosmic-ray induced neutron burn-out of the ^{182}W nuclide relative to the normalizing isotopes. Leya et al. (2003) reported the most detailed calculations of the effect of neutron burn-out on $\epsilon^{182}\text{W}$, including effects on the normalizing isotopes, and Kleine et al. (2005a) applied the calculations to show that none of their iron meteorite data could have been lowered by more than $\Delta\epsilon^{182}\text{W} \sim 0.3$ units. Markowski et al. (2006a) obtained a more precise estimate of the cosmic-ray fluence experienced by iron meteorites by performing tungsten isotope measurements on samples for which ^3He abundances were simultaneously determined. They concluded that, after correction for neutron fluence, the $\epsilon^{182}\text{W}$ of these iron meteorites (-3.47 ± 0.35 , 2σ) was within error of the Kleine et al. (2005a) CAI initial $\epsilon^{182}\text{W} = -3.47 \pm 0.20$ (2σ) implying segregation of iron cores in the four magmatic iron meteorite groups represented by these meteorites (IIAB, IID, IIIAB, and IVB) within <1 m.y. of CAI formation (Mar-

kowski et al., 2006a). In the first six million years of solar system history, the rate of change of $\epsilon^{182}\text{W}$ is about 0.1 ϵ units/m.y. using the parameters of Kleine et al. (2005a). Even small downward revisions of the solar system initial value then increase the ^{182}Hf – ^{182}W ages of magmatic iron meteorites by several million years. This is important given that ^{26}Al heating occurs largely within the first 5 m.y. of solar system history (e.g., Humayun and Campbell, 2002). We, therefore, urge the analysis of ^{182}Hf – ^{182}W in CAIs from the reduced CV3 subgroup (e.g., Efremovka), because their CAIs have undergone less alteration, to soundly distinguish between the possibilities that we have identified here. Given the importance of the solar system initial $\epsilon^{182}\text{W}$ value, the sacrifice of several large CAIs from Efremovka, Leoville, and Vigarano will be justified to obtain a value that cannot be arguably impacted by parent body processes. The present work has provided the necessary information on the Hf and W distributions in CAIs that should guide the effective mineral separations needed for future Hf–W measurements of the least radiogenic $\epsilon^{182}\text{W}$ of the solar system.

5. CONCLUSIONS

We have determined by laser ablation ICP-MS the distribution of Hf and W in two CAIs: Ef2, a Compact Type A from Efremovka (CV3 reduced), and Golfball (GBS), a Type B from Allende (CV3 oxidized). The primary host of Hf in both CAIs is fassaite, which is zoned with relatively Hf-rich cores to Hf-poor rims correlated with TiO_2 in an approximately chondritic ratio. The Hf content of the fassaite core in GBS is ~ 14 ppm, and that for Ef2 is ~ 20 ppm. No other phase was found to contain measurable Hf. The primary phase hosting W in Ef2 is Fe–Ni alloy, and in GBS is opaque assemblages (OAs) derived by alteration of Fe–Ni alloy. Abundant inclusions of Fe–Ni alloy, or OAs, are found associated with melilite, fassaite, and spinel, so that W abundances in bulk samples of these phases range from 0.003 to ~ 100 ppm. The W abundances in silicates and oxides correlate with Pt abundances in both Efremovka Ef2 and Allende GBS. Fassaite from both CAIs has $^{180}\text{Hf}/^{184}\text{W} > 10$ in the majority of analyses, with the cleanest fassaite yielding $^{180}\text{Hf}/^{184}\text{W} > 3700$ (Ef2) and > 1800 (GBS). Melilite in both CAIs had $^{180}\text{Hf}/^{184}\text{W} < 1$. Since melilite has no measurable Hf, the presence of metallic particles contributing W makes melilite a potential mineral separation target for determining the initial $\epsilon^{182}\text{W}$ in CAIs.

Direct measurement of the elemental abundances in EM2, a large ($\sim 300 \mu\text{m}$) Fe–Ni alloy particle in Ef2, shows < 0.2 ppm Hf with $^{180}\text{Hf}/^{184}\text{W} < 0.006$. The Sc and Y abundances were also below detection limits, while Ti (~ 9 ppm) and Ta (~ 3 ppm) were detected. The Ta abundance was high enough to make metal an important host of Ta, since the concentration of Ta was found to be lower in fassaite (< 1 ppm), and below the detection limit (< 0.003 ppm) in melilite. Secondary processes have altered the primary Fe–Ni alloy in Allende GBS to form veins containing oxidized W. The mobility of W demonstrated in GBS compromises the use of Allende CAIs for determining the initial

$\epsilon^{182}\text{W}$ of the solar system since it reveals that the CAIs were open systems with respect to W.

There are two possible interpretations of the existing Allende CAI ^{182}Hf – ^{182}W data of Kleine et al. (2005a):

- (i) the CAIs were open systems for water and sulfur, but dominated the local W budget so that secondary W is isotopically representative of the primary metal; or
- (ii) redistribution of W during formation of OAs followed by metamorphism resulted in rotation of the CAI isochron, so that the present $\epsilon^{182}\text{W}$ is more radiogenic than the solar system initial $\epsilon^{182}\text{W}$.

It is not possible to discriminate between these models on the basis of existing information, but sensitive *in situ* determination of ^{182}Hf – ^{182}W systematics could potentially discriminate between these alternatives if complete isotopic equilibration of W in CAIs did not occur. Because of the great importance of knowing the solar system initial $\epsilon^{182}\text{W}$ for the use of ^{182}Hf – ^{182}W chronometry it is imperative to determine the solar system initial $\epsilon^{182}\text{W}$ from CAIs in the reduced CV3 subgroup (Efremovka, Leoville, and Vigarano), which tend to be much less altered than those from the oxidized CV3 subgroup. Only then will it be possible to determine accurate ages of differentiation of iron meteorites, which currently appear to have formed < 1 m.y. after the formation of CAIs (Kleine et al., 2005a; Markowski et al., 2006a,b). The accurate application of the ^{182}Hf – ^{182}W chronometer to iron meteorites requires an equally accurate value of the solar system's initial $\epsilon^{182}\text{W}$. The effect of nucleosynthetic anomalies in iron meteorites on the interpretation of ^{182}Hf – ^{182}W ages remains to be fully considered.

ACKNOWLEDGMENTS

Discussions with Alan Treiman, Kevin Righter, Thorsten Kleine, and Agnes Markowski were very helpful. We thank Herbert Palme and Qingzhu Yin for their thorough and constructive reviews. We thank Alan Brandon for his comments and editorial handling of the manuscript. Funding for this research was provided by the NASA Cosmochemistry program (Science Mission Directorate) under Grants NNG05GB81G and NNG06GF50G (M.H.) and NNG05GG00G (L.G.), for which we are very thankful.

REFERENCES

- Amelin Y., Krot A. N., Hutcheon I. D. and Ulyanov A. A. (2002a) Lead isotopic ages of chondrules and calcium–aluminum-rich inclusions. *Science* **297**, 1678–1683.
- Amelin, Y., Grossman, L., Krot, A. N., Pestaj, T., Simon, S. B. and Ulyanov, A. A. (2002b) U–Pb age of refractory inclusions from the CV carbonaceous chondrites Allende and Efremovka. *Lunar Planet. Sci. XXXIII*, LPI, Houston (CD-ROM). #1151 (abstr.).
- Anders E. and Grevesse N. (1989) Abundances of the elements: meteoritic and solar. *Geochim. Cosmochim. Acta* **53**, 197–214.
- Beckett J. R., Live D., Tsay F.-D., Grossman L. and Stolper E. (1988) Ti^{+3} in meteoritic and synthetic hibonite. *Geochim. Cosmochim. Acta* **52**, 1479–1495.

- Bischoff A. and Palme H. (1987) Composition and mineralogy of refractory-metal-rich assemblages from a Ca,Al-rich inclusion in the Allende meteorite. *Geochim. Cosmochim. Acta* **51**, 2733–2748.
- Blum J. D., Wasserburg G. J., Hutcheon I. D., Beckett J. R. and Stolper E. M. (1989) Origin of opaque assemblages in C3V meteorites: implications for nebular and planetary processes. *Geochim. Cosmochim. Acta* **53**, 543–556.
- Brandon A. D., Humayun M., Puchtel I. S., Zolensky M. and Leya I. (2005) Osmium isotope evidence for an s-process carrier in primitive chondrites. *Science* **309**, 1233–1236.
- Campbell A. J. and Humayun M. (1999) Trace element microanalysis in iron meteorites by laser ablation ICPMS. *Anal. Chem.* **71**, 939–946.
- Campbell A. J. and Humayun M. (2003) Formation of metal in GRO 95551 and comparison to ordinary chondrites. *Geochim. Cosmochim. Acta* **67**, 2481–2495.
- Campbell A. J. and Humayun M. (2004) Formation of metal grains in the CH chondrites ALH 85085 and PCA 91467. *Geochim. Cosmochim. Acta* **68**, 3409–3422.
- Campbell A. J. and Humayun M. (2005) Compositions of Group IVB iron meteorites and their parent melt. *Geochim. Cosmochim. Acta* **69**, 4733–4744.
- Campbell A. J., Humayun M., Meibom A., Krot A. N. and Keil K. (2001) Origin of zoned metal grains in the QUE94411 chondrite. *Geochim. Cosmochim. Acta* **65**, 163–180.
- Campbell A. J., Humayun M. and Weisberg M. K. (2002) Siderophile element constraints on the formation of metal in the metal-rich chondrites Bencubbin, Weatherford, and Gujba. *Geochim. Cosmochim. Acta* **66**, 647–660.
- Campbell A. J., Simon S. B., Humayun M. and Grossman L. (2003) Chemical evolution of metal in refractory inclusions in CV3 chondrites. *Geochim. Cosmochim. Acta* **67**, 3119–3134.
- Campbell A. J., Humayun M. and Weisberg M. K. (2005) Compositions of unzoned and zoned metal in the CB₆ chondrites Hammadah al Hamra 237 and Queen Alexandra Range 94627. *Meteorit. Planet. Sci.* **40**, 1131–1148.
- Chen, J. H., Papanastassiou, D. A., Wasserburg, G. J. and Ngo, H. H. (2004) Endemic Mo isotopic anomalies in iron and carbonaceous meteorites. *Lunar Planet. Sci. XXXV*, LPI, Houston (CD-ROM). #1431 (abstr.).
- Eisenhour D. D. and Buseck P. R. (1992) Transmission electron microscopy of RMNs: implications for single-phase condensation of the refractory siderophile elements. *Meteoritics* **27**, 217–218.
- El Goresy A., Nagel K. and Ramdohr P. (1978) Fremdlinge and their noble relatives. *Proc. Lunar Planet. Sci. Conf.* **9**, 1279–1303.
- Fisenko A. V., Ignatenko K. I. and Lavrukina A. K. (1992) The metallic phase in a type B1 CAI fragment in the Yefremovka CV chondrite. *Geochim. Int.* **29**, 85–93.
- Gray C. M., Papanastassiou D. A. and Wasserburg G. J. (1973) The identification of early condensates from the solar nebula. *Icarus* **20**, 213–239.
- Grossman L. (1972) Condensation in the primitive solar nebula. *Geochim. Cosmochim. Acta* **36**, 597–619.
- Grossman L. and Ganapathy R. (1976) Trace elements in the Allende meteorite-I. Coarse-grained, Ca-rich inclusions. *Geochim. Cosmochim. Acta* **40**, 331–344.
- Guimon R. K., Symes S. J., Sears D. W. G. and Benoit P. H. (1995) Chemical and physical studies of type 3 chondrites XII: the metamorphic history of CV chondrites and their components. *Meteoritics* **30**, 704–714.
- Harper, Jr., C. L. and Jacobsen S. B. (1996) Evidence for ¹⁸²Hf in the early solar system and constraints on the timescale of terrestrial accretion and core formation. *Geochim. Cosmochim. Acta* **60**, 1131–1153.
- Herzog, G. F. (2006) Cosmic-ray exposure ages of meteorites. In *Treatise in Geochemistry*, vol. 1, Meteorites, Comets, and Planets (eds. A. M. Davis, H. D. Holland and K. K. Turekian). Elsevier, New York.
- Humayun M. and Campbell A. J. (2002) The duration of ordinary chondrite metamorphism inferred from tungsten microdistribution in metal. *Earth Planet. Sci. Lett.* **198**, 225–243.
- Humayun, M. and Campbell, A. J. (2003) Microanalysis of niobium in iron meteorites. *Lunar Planet. Sci. XXXIV*, LPI, Houston (CD-ROM). #1480 (abstr.).
- Humayun, M., Simon, S. B. and Grossman, L. (2006) Tungsten and hafnium distribution in calcium–aluminum inclusions (CAIs) from Allende and Efremovka. *Lunar Planet. Sci. XXXVII*, LPI, Houston (CD-ROM). #2338 (abstr.).
- Jochum K. P. and 35 coauthors (2000) The preparation and preliminary characterization of eight geological MPI-DING reference glasses for in-situ microanalysis. *Geostandards Newsl.* **24**, 87–133.
- Jochum K. P. and 52 coauthors (2006) MPI-DING reference glasses for in situ microanalysis: new reference values for element concentrations and isotope ratios. *Geochim. Geophys. Geosyst.* **7**, Q02008. doi:10.1029/2005GC00106, 44 pp.
- Kleine T., Münker C., Mezger K. and Palme H. (2002) Rapid accretion and early core formation on asteroids and the terrestrial planets from Hf–W chronometry. *Nature* **418**, 952–955.
- Kleine T., Mezger K., Palme H., Scherer E. and Münker C. (2005a) Early core formation in asteroids and late accretion of chondrite parent bodies: evidence from ¹⁸²Hf–¹⁸²W in CAIs, metal-rich chondrites, and iron meteorites. *Geochim. Cosmochim. Acta* **69**, 5805–5818.
- Kleine T., Palme H., Mezger K. and Halliday A. N. (2005b) Hf–W chronometry of lunar metals and the age and the early differentiation of the Moon. *Science* **310**, 1671–1674.
- Krot A. N., Hutcheon I. D., Brearley A. J., Pravdivtseva O. V., Petaev M. I. and Hohenberg C. M. (2006) Timescales and settings for alteration of chondritic meteorites. In *Meteorites and the Early Solar System II* (eds. D. S. Lauretta and H. Y. McSween Jr). University of Arizona Press, Tucson, pp. 525–553.
- Lee D.-C. and Halliday A. N. (1996) Hf–W isotopic evidence for rapid accretion and differentiation in the early solar system. *Science* **274**, 1876–1879.
- Leya I., Wieler R. and Halliday A. N. (2000) Cosmic-ray production of tungsten isotopes in lunar samples and meteorites and its implications for Hf–W cosmochemistry. *Earth Planet. Sci. Lett.* **175**, 1–12.
- Leya I., Wieler R. and Halliday A. N. (2003) The influence of cosmic-ray production on extinct radionuclide systems. *Geochim. Cosmochim. Acta* **67**, 529–541.
- Markowski A., Leya I., Quitté G., Ammon K., Halliday A. N. and Wieler R. (2006a) Correlated helium-3 and tungsten isotopes in iron meteorites: quantitative cosmogenic corrections and planetesimal formation times. *Earth Planet. Sci. Lett.* **250**, 104–115.
- Markowski A., Quitté G., Halliday A. N. and Kleine T. (2006b) Tungsten isotopic compositions of iron meteorites: chronological constraints vs. cosmogenic effects. *Earth Planet. Sci. Lett.* **242**, 1–15.
- Palme H., Hutcheon I. D. and Spettel B. (1994) Composition and origin of refractory-metal-rich assemblages in a Ca,Al-rich Allende inclusion. *Geochim. Cosmochim. Acta* **58**, 495–513.
- Papanastassiou D. A., Chen J. H. and Wasserburg G. J. (2004) More on Ru endemic isotope anomalies in meteorites. *Lunar Planet. Sci. XXXV*, LPI, Houston (CD-ROM). #1828 (abstr.).

- Pearce N. J. G., Perkins W. T., Westgate J. A., Gorton M. P., Jackson S. E., Neal C. R. and Chenery S. P. (1997) A compilation of new and published major and trace element data for NIST SRM 610 and NIST SRM 612 glass reference materials. *Geostandards Newsl.* **21**, 115–144.
- Scherer P. and Schultz L. (2000) Noble gas record, collisional history, and pairing of CV, CO, CK, and other carbonaceous chondrites. *Meteorit. Planet. Sci.* **35**, 145–153.
- Simon S. B., Grossman L. and Davis A. M. (1991) Fassaite composition trends during crystallization of Allende Type B refractory inclusion melts. *Geochim. Cosmochim. Acta* **55**, 2635–2655.
- Simon S. B., Grossman L. and Davis A. M. (2005) A unique type B inclusion from Allende with evidence for multiple stages of melting. *Meteorit. Planet. Sci.* **40**, 461–475.
- Sylvester P. J. and Eggins S. M. (1997) Analysis of Re, Au, Pd, Pt and Rh in NIST glass certified reference materials and natural glasses by laser ablation ICP-MS. *Geostandards Newsl.* **21**, 215–229.
- Sylvester P. J., Grossman L. and MacPherson G. J. (1992) Refractory inclusions with unusual chemical compositions from the Vigarano carbonaceous chondrite. *Geochim. Cosmochim. Acta* **56**, 1343–1363.
- Sylvester P. J., Simon S. B. and Grossman L. (1993) Refractory inclusions from the Leoville, Efremovka, and Vigarano C3V chondrites: major element differences between Types A and B, and extraordinary refractory siderophile element composition. *Geochim. Cosmochim. Acta* **57**, 3763–3784.
- Wasson J. T., Ouyang X., Wang J. and Jerde E. (1989) Chemical classification of iron meteorites: XI. Multi-element studies of 38 new irons and the high abundance of ungrouped irons from Antarctica. *Geochim. Cosmochim. Acta* **53**, 735–744.
- Yin Q., Jacobsen S. B., Yamashita K., Blichert-Toft J., Télouk P. and Albarede F. (2002) A short timescale for terrestrial planet formation from Hf–W chronometry of meteorites. *Nature* **418**, 949–952.

Associate editor: Alan D. Brandon